Monte Carlo simulations of the iThemba LABS neutron beam facility

BUTHAINA ABDALLA SULEIMAN ADAM

A thesis submitted to University of Cape Town in
requirements for the Degree of
Master of Science

November 18, 2010

Abstract

The iThemba LABS neutron beam facility is currently being used for various applications of fast neutron studies, such as measurements of fission cross sections, the biological effectiveness of high-energy neutrons, calibration of detectors used for dose monitoring in space and aircrafts, and the development of neutron dose monitors.

Neutron beams with energies up to 200 MeV are produced at iThemba LABS by irradiating thin targets of ^{7}Li and ^{9}Be with protons from the separated-sector cyclotron. The neutrons are collimated to produce a beam with a diameter of about 50 mm at a flight path of 7.7 m from the target. The collimator geometry is designed to maximize the central part of the beam resulting in a beam with a uniform intensity throughout its diameter and a small penumbra. Secondary neutrons produced from the interactions of the primary charged particles with structural parts e.g. beampipes, shielding wall, target holder, etc have been observed in the measured neutron fluence spectra. The Monte Carlo radiation transport code FLUKA were used to study the effects of secondary neutrons on the neutron fluence spectra. Results obtained from the calculations were compared with those obtained experimentally.

Declaration

I know the meaning of plagiarism and declare that all of the work in the document, save for that which is properly acknowledged, is my own.

---------- ----------

Adam Buthaina Date

Acknowledgment

I would like to express my deepest gratitude to Dr. Rudolph Nchodu and Dr. Zinhle Buthelezi for their belief in me, patience, guidance and all the support they have given me during my years as a MSc student. I also want to thank you for the help I received to understand the art of scientific research, nuclear physics and Monte Carlo simulation. Finally I want to thank you for the time you spent in order to get this project to the point were it is today, thank you.

I would like to express my profound gratitude to African institute for mathematical sciences (AIMS) for giving me the opportunity to be in South Africa and started my carrier as a scientist. Special thanks also goes to my friends who supported me in one way or the other, Mark Herbert, Emmanuel Jonah, Sara Abass, Mohammed Yagoob, Maye Elmardi, Hussam Mohammed, Salma Elkhair, Maisson Mattar, labo, you guys helped me a lot, wish you all the best.

I also appreciate the Sudan Atomic Energy Commission family, particularly, Dr Adam Sam, my friends: Nada and Sulafa. I am indebted to my Mum, **Haleima** and all my brothers Abbaker, Mohammed, Ahmed, Haroon, Elsadig, Hafiz, Adam, Alaa Eldien and Khalid for giving me the necessary encouragement and social support, I love you.

Finally, I would like to take this opportunity to express my gratitude and thank my husband **Ibrahim Suleiman** for his love and moral support during my study. He is both a comfort and an inspiration, You are the reason I have succeeded so far, and strive to do so in the future, thanks and I love you.

May God bless you all

Dedication

To my mother for her care, patience, understanding, support, encouragement and most of all her love.

To my father, may his soul rest in peace.

Contents

Chapter 1

Introduction

The iThemba Laboratory for Accelerator-Based Sciences (iThemba LABS) is the laboratory for multidisciplinary particle accelerator research in Faure, near Cape Town in South Africa. It provides facilities for basic applied research using accelerated particle beams, radiotherapy for the treatment of cancer and supply accelerator-produced radioactive isotopes for nuclear medicine and research [1].

The neutron facility at iThemba LABS is used for neutron physics studies [2] as well as applications such as radiobiology (the investigation of the biological effect) [3], radiation dosimetry (testing instruments at high energy accelerators), measurements of cross sections for neutron induced reactions [4], and calibration of detectors used for dose monitoring in space and aircrafts [5]. A characterized mono-energetic neutron beam is needed for the above mentioned applications. Experimentally a mono-energetic beam cannot be produced, only quasi-monoenergetic neutron beam because of the contribution of the secondary neutrons as well as neutrons produced due to the nature of the interaction between the incident protons and the target. Quasi-monoenergetic neutron beams are useful for calibrating detectors which are not able to distinguish between several neutron energies, this can be done by using different methods one of which is Time-Of-Flight (TOF) [5].

The beam line at the neutron facility consists of several components such as concrete, iron, borated polyethylene, etc, which are used to provide a well collimated beam in the experimental area (see section 1.1 for more details). When neutrons interact with these materials, they usually

produce secondary types of radiation such as photons and neutrons as a by-product of inelastic scattering, i.e. (n,n')-reactions, as well as capture gamma photons from (n, γ) reactions. Neutrons can interact in different ways depending on the scattering cross section interaction and the larger this cross-section the more interactions there will be, which results in more secondary particles being produced (secondary neutrons) (see Fig. 1.12). There have been observations of secondary neutrons which affect the spectral distribution of the neutron beams by increasing the low energy component [6, 7]. These secondary neutrons may have been produced from the interactions of the primary charged particles with structural parts, e.g. beampipes, shielding wall, target holder, collimator, etc. Secondary neutrons, may escape through the passage from the target area to the experimental area (see Fig. 1.2). In order to understand where in the beam line secondary neutron scattering is taking place, it is necessary to model the neutron facility in its entirety and obtain the neutron fluence spectra for the entire energy range. In principle, neutron fluence spectra can be measured experimentally or calculated using Monte Carlo radiation transport codes [8, 9]

1.1 iThemba LABS neutron facility

At iThemba LABS a separated-sector cyclotron (SSC) and its two injector cyclotrons can accelerate different types of beams such as light and heavy ions as well as the polarized proton ions which are produced in the polarized ion source. Proton beam which is used for production of the neutrons is pre-accelerated in the first solid-pole injector cyclotron (SPC1) to energy of 3.14 MeV and then accelerated finally in SSC up to energy 200 MeV [10, 11]. The layout of the accelerator facilities at iThemba LABS is shown in Fig. 1.1. A proton beam of energy up to 200 MeV is then transported into D-line vault where the neutron time of flight facility is situated. Fig. 1.2 shows schematic diagram of the neutron facility at iThemba LABS.

Neutron beams are produced at iThemba LABS in the time-of-flight facility through different reactions such as ^{7}Li(p,n)^{7}Be and ^{9}Be(p,n)^{9}B. As can be seen in Fig. 1.2 the incoming protons interact with the target and the neutrons produced are emitted via the 3 m long circular iron collimator (25 mm diameter) at several neutron emission angles (0°, 4°, 8°, 12° and 16°). The neutron flight paths used in this facility can be extended from about 5 m to about 10 m. The 0°

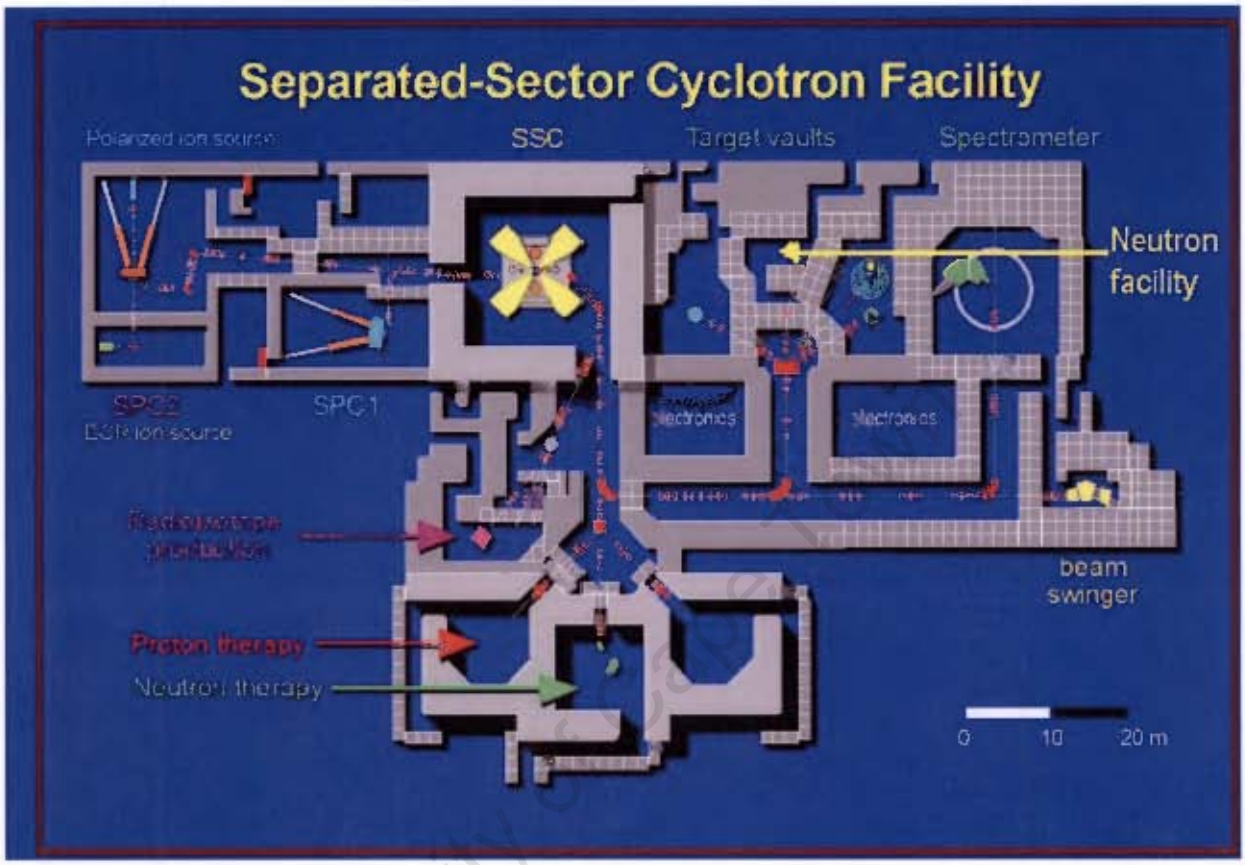

Figure 1.1: Layout of iThemba LABS

collimator is located at a distance of 2 m away from the target. Unwanted charged particles are directed to the beam dump and a 5 cm x 5 cm graphite block is inserted inside the collimator to absorbed residual charged particles that did not pass through the beam dump. Two doors are located at the end of the passage to separate the area where neutrons are produced and the experimental area. The first door from the side of production area is composed of iron while the other one is made of borated polyethylene, in order to prevent the scattered neutrons that might escape through the passage into the measurement area. There is a small opening with a height of about 150 cm and 77 cm width above these doors i.e. space between the doors and the concrete blocks forming part of the ceiling.

Neutron beams produced from 100 MeV protons incident on a 5 mm thick ^{7}Li target at iThemba LABS are characterized for 0° and 16° neutron emission angles [5] by a high energy peak and the continuum neutron spectrum (tail). Fig. 1.3 shows the fluence spectra measured at iThemba

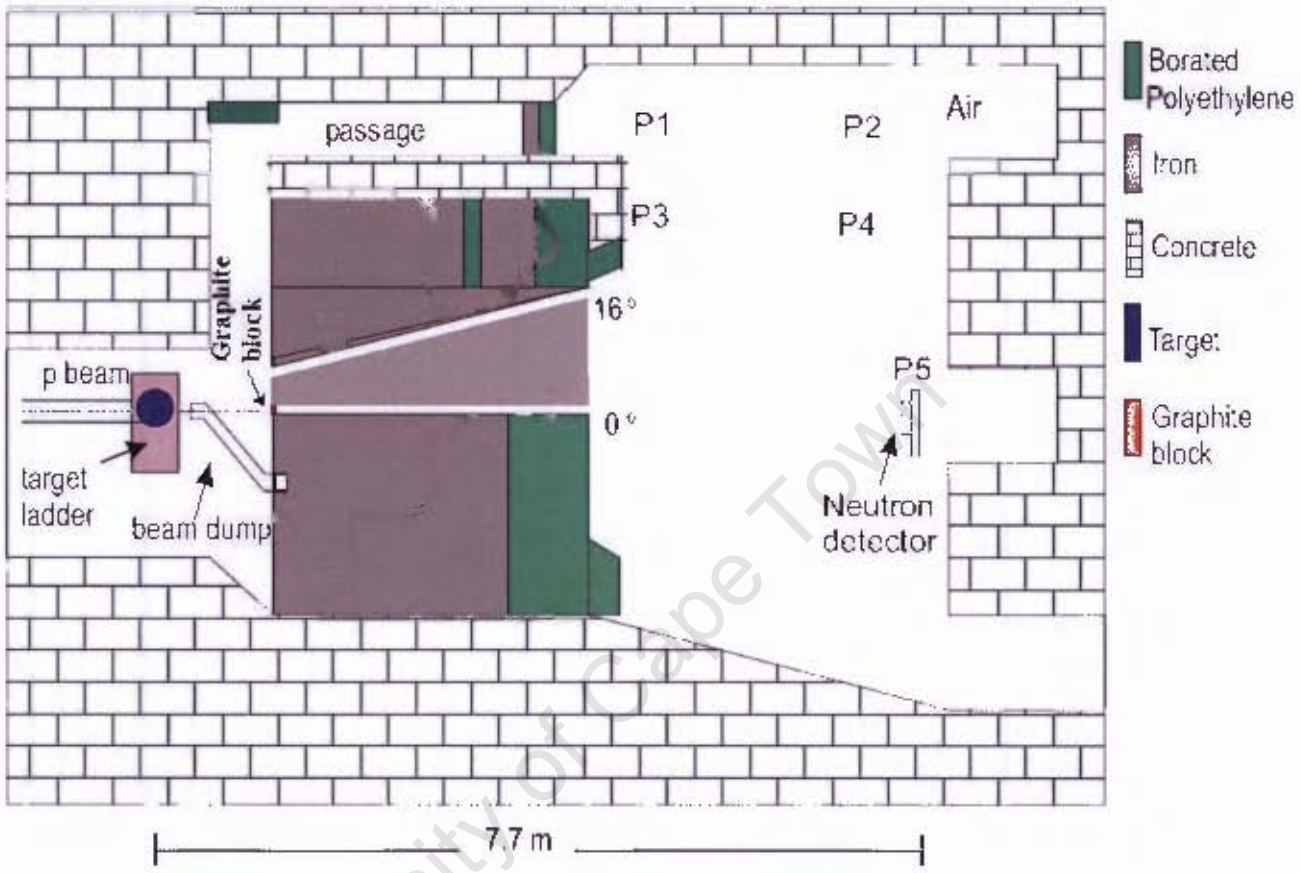

Figure 1.2: Schematic representation of iThemba LABS neutron facility.

I ABS where quasi monoenergetic neutrons were obtained by bombarding a thin ^{7}Li target with 100 MeV protons. The neutron fluence, f, can be defined as the neutron flux[1], ϕ, integrated over the entire measurement time, t, and represents the number of neutrons per unit area that passed during this time.

$$f = \int_0^t \phi(t)dt. \tag{1.1}$$

Neutron fluence spectrum obtained at 0° shown in the figure, consists of two parts, a high energy peak and a continuum neutron spectrum [5]. The high energy peak results from the ground state transition of the ^{7}Li(p,n)^{7}Be reaction, and the first excited state, while the continuum neutron spectrum (tail) is the spectrum results from the breakup reactions and secondary neutrons.

[1]Neutron flux: is the number of neutrons passing through a unit area in unit time.

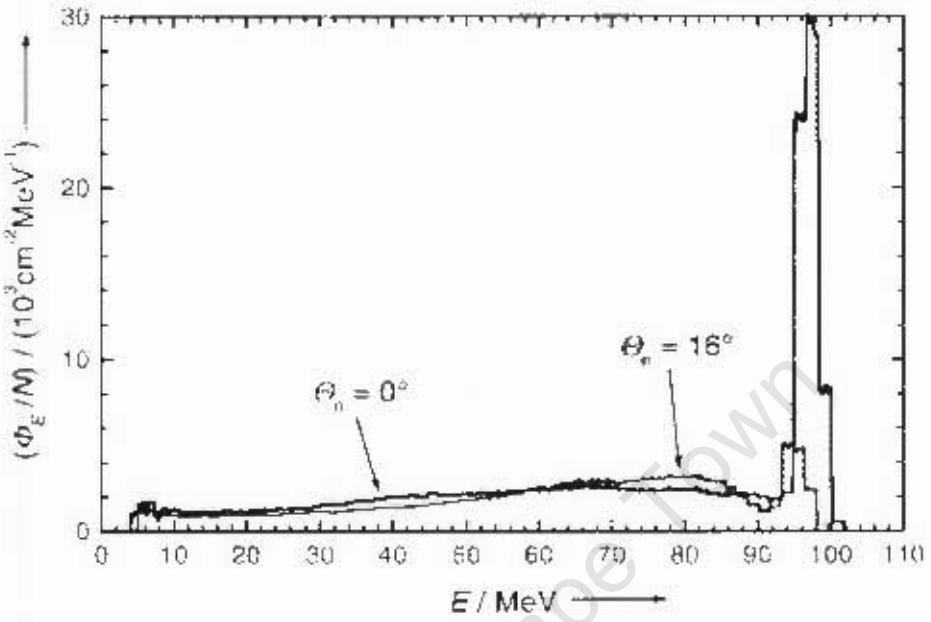

Figure 1.3: Measured neutron fluence spectra for ^{7}Li(p,n)^{7}Be reaction at neutron emission angles of 0° (thick line) and 16° (thin line) relative to the proton beam direction [5].

1.2 Neutron fluence measurements

Neutron fluence spectra can be measured using a variety of methods based on different techniques such as recoil spectrometry, Time-of-Flight (TOF) [12], threshold spectrometry and methods based on neutron moderation [13]. The recoil spectrometry involves measurement of the recoiling nucleus energy after the neutron is scattered off the nucleus, e.g. recoil proton telescope [14]. The TOF technique is based on measuring the neutron flight times over well defined distances and then converting the obtained flight times to energies. Threshold spectrometry in which a minimum neutron energy is indicated by the appearance of a neutron induced effect such as radioactivity (activation or fission [15, 13]). In this work, the method based on TOF technique was used to obtain the neutron fluence because the measurements were made using organic scintillator which has a fast time response and is well suited for timing measurements.

Organic scintillation detectors are the most common detectors used for fast neutron detection where neutron undergo elastic scattering of hydrogen and detected, indirectly, via secondary charged particles released in the interaction with the scintillation components. Energy deposited by charged particles is converted into an electrical pulse by a photomultiplier tube. The height or

the amplitude of this pulse is proportional to the total light produced in the scintillator. Organic scintillators have a fast time response and are well suited for timing measurements. The rise time, i.e. the time it takes to populate the prompt fluorescence levels, is the order of 0.5-1.0 ns for most organic scintillators, and decay times range from 2 to 4 nanosecond (ns) [16, 17]. In addition, some scintillators have a slower decay component and the number of the particles of these slower decaying levels depends on the particle type as shown in Fig.1.4.

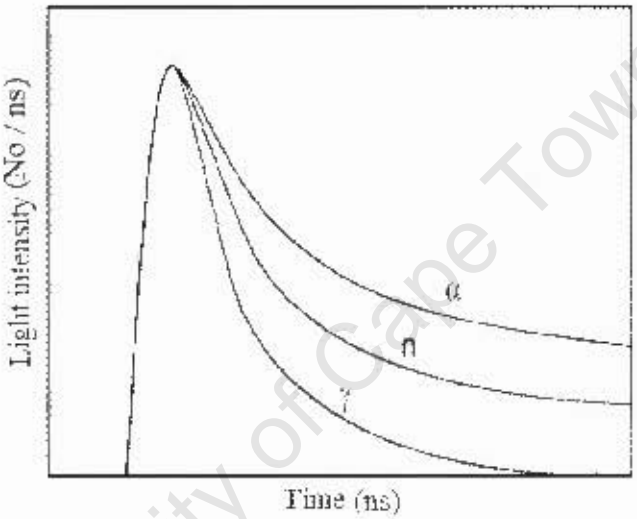

Figure 1.4: Time dependence of scintillation pulses in a detector when excited to different types of radiation [16].

Fig. 1.5 shows a schematic diagram of the main electronic configuration of components used for pulse processing. The pulses may be plotted in energy distributions called pulse height spectra. Generally, the signals from scintillators are the sum of two exponential decays (fast and slow signal), which carry information in their shape, or more precisely in their rise and decay time. Particles of different ionization powers produce longer or shorter pulses in the detector, resulting in different pulse shapes [17, 16]. A pulse shape analyzer, such as LINK module [18] can be used to produce the pulse height L, by integrating the input pulse over a long period (500 ns) and fast component F, by integrating the input pulse over a short period (about 30ns) [19, 20].

A flow chart representing the different steps used for neutron fluence measurement is shown in Fig. 1.6. The timing signal is used to start the Time-to-Amplitude Converter (TAC) that measured the neutron time-of-flight, T, the stop pulse for TAC is provided by the beam pulse. The TOF, T, can be calibrated into the neutron energy, E_n. The pulse height, L, can be used

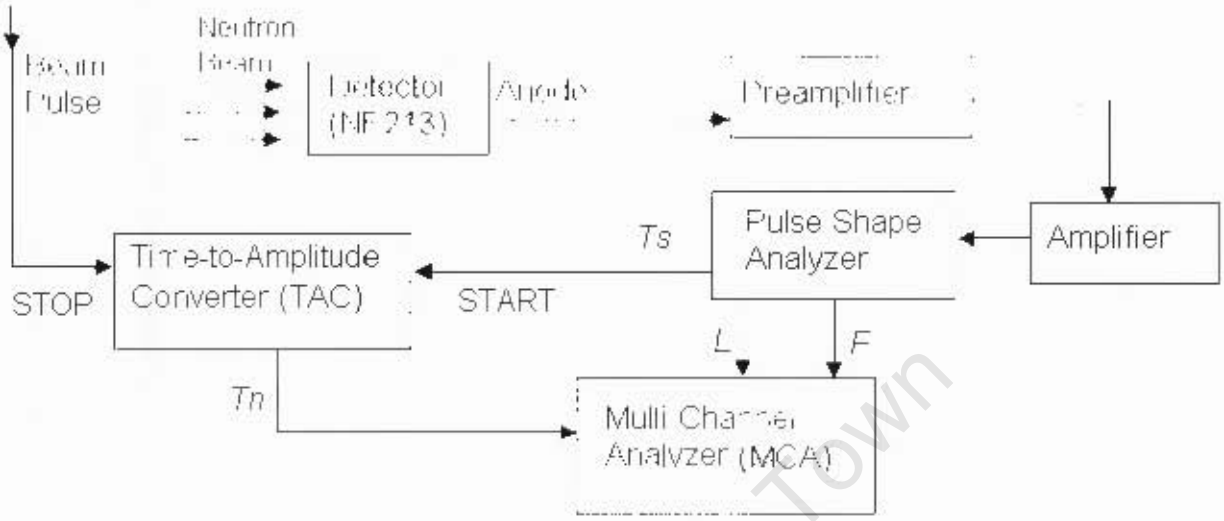

Figure 1.5: Schematic diagram of the main electronic configuration of components used for the pulse processing T_n measure, the flight times of the neutrons from the target to front of the scintillator, L is the pulse height and F is the fast component of the pulse height.

with the neutron energy, E_n, to determine the efficiency of the detector. The efficiency of the detector, as a function of the neutron energy, is an important property of the detector that needs to be determined (experimentally or calculated using Monte Carlo code) in order to determine the total number of the neutrons that interact with the scintillator material in the detector medium. Neutron fluence at a particular energy can be measured from the total number of neutrons and the cross sectional area of the detector using the fluence equation

$$\Phi = \frac{N_o}{A}, \tag{1.2}$$

where Φ is the neutron fluence, N_o is the total neutron number and A is the cross sectional area of the detector.

1.2.1 Detector response function

The pulse height spectrum measured for a neutron of a specific energy using an organic scintillation detector is known as the response function of the scintillator. The response function depends on the energy of the incident neutron, the type of the interactions in the detector, and the geometry of the detector. Its measurements are, therefore, made at various incident neutron energies

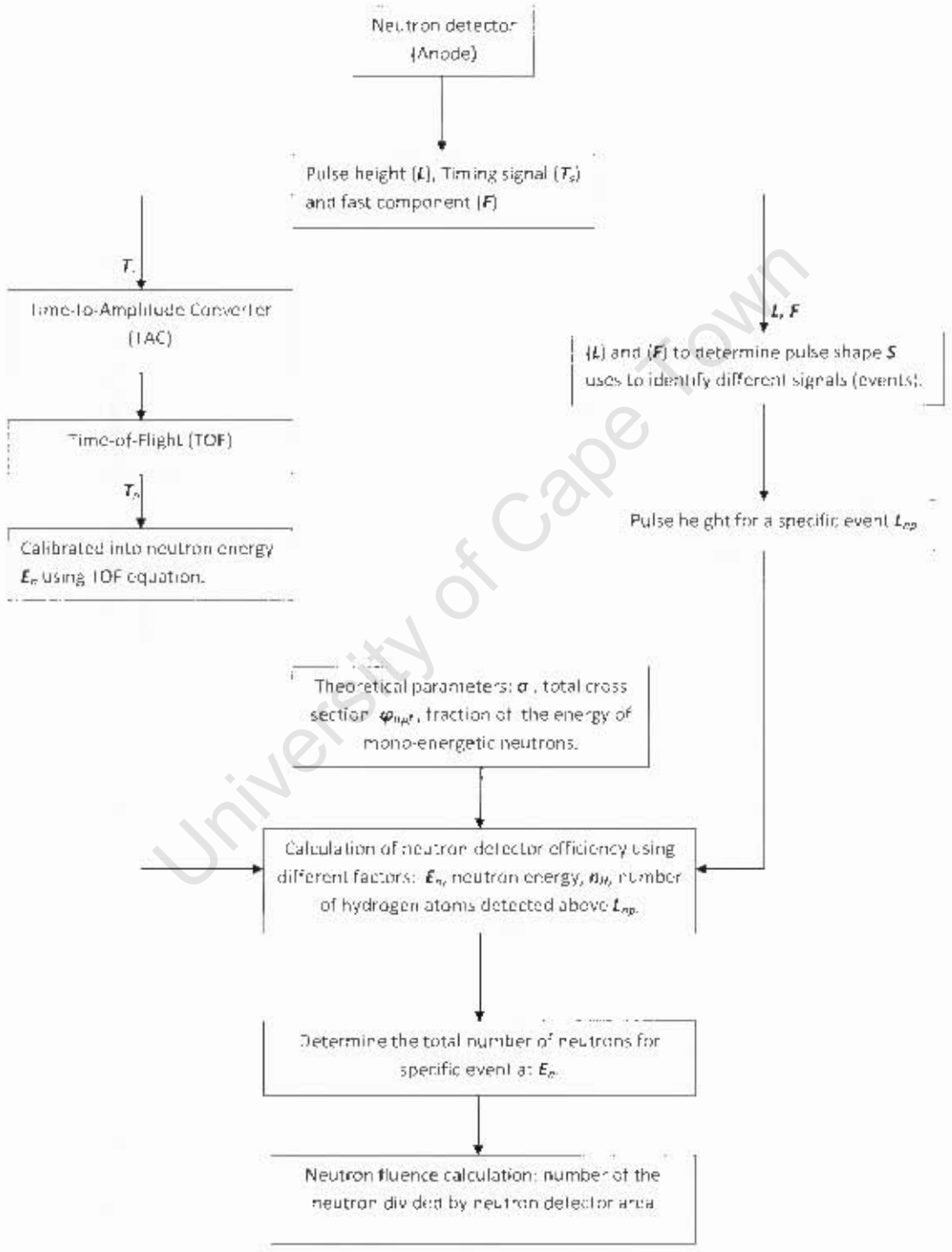

Figure 1.6. A flow chart showing the different steps to measure neutron fluence using TOF technique, see text for details.

[21, 22, 23, 24]. Below 20 MeV, the response functions have been measured experimentally and well reproduced by Monte Carlo calculations. On the other hand, in an energy range above 20 MeV, fewer measurements and calculations of the response functions in several-tens-MeV neutron energy region have been reported [25, 26, 27].

An ideal or the expected distribution of proton recoil energy from a mono-energetic neutron source is a simple rectangle as shown in Fig.1.7 where the probability for a neutron interacting in the detector volume is equal for all energies. However, in a real detector many different factors contribute to the formation of the measured spectrum such as edge effect, multiple hydrogen scattering and nonlinear light output [16]. Edge effect is caused by incomplete energy deposition

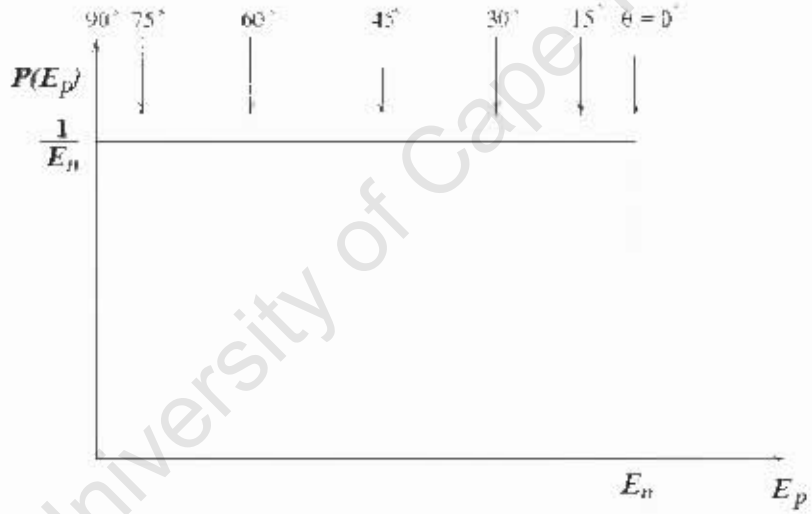

Figure 1.7: Ideal energy distribution of the recoil proton from a mono-energetic neutron source [16].

by the recoil charged particles (protons). When the energy of the neutron is high, i.e. it has sufficient energy such that the recoil proton's mean free path is large in comparison with the detector dimensions, then edge effect will be observed in the detector output [16].

Neutrons may undergo multiple hydrogen or carbon scatterings before stopping within the detector volume. If a neutron undergoes multiple carbon scatterings, then the resulting spectrum would be similar to that resulting from a single carbon event, where more low energy events will be observed. On the other hand, if the neutron undergoes multiple hydrogen scatterings, the effect could be significant in the resulting spectrum. All events from a single neutron, even from multiple scatterings, happen within a short period of time and will be recorded as one event in the final

spectrum. Since the average energy lost in a single neutron hydrogen collision is half of the neutron's initial energy, multiple scatterings with hydrogen increases the energy transferred to the detector and causes more high energy events to be observed [16, 28, 29]. Response of an organic scintillator to protons may be obtained from the upper limit of the pulse height spectrum of recoil protons produced by elastic n-p scattering of mono-energetic neutrons in the scintillator. Effect of the different factors which contribute to the formation of the pulse height spectrum can be seen clearly in Fig. 1.8.

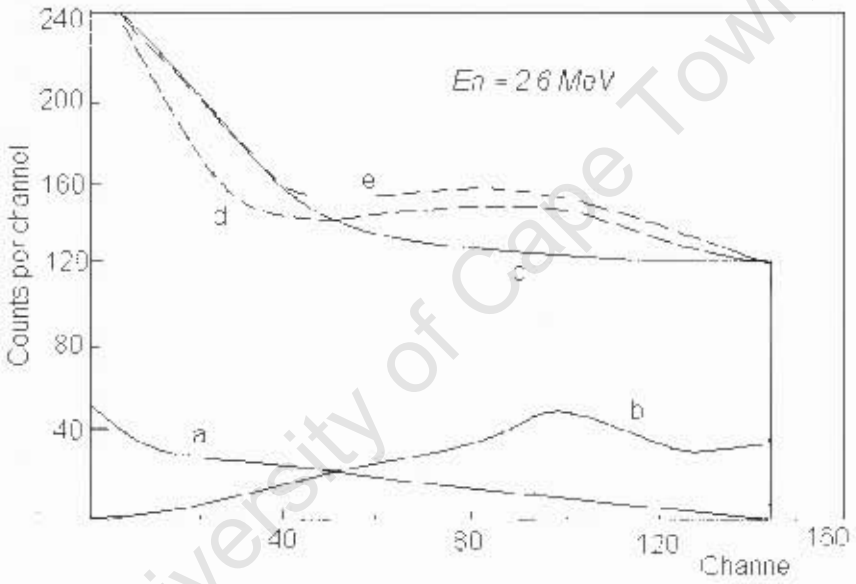

Figure 1.8: The different factors affecting the response function calculated for a cylindrical stilbene crystal at neutron energy of 2.6 MeV. a: multiple carbon scattering, b: multiple hydrogen scattering, c: single scattering with detector nonlinearity and edge effect, d: combination of single and multiple scattering from hydrogen, e: composite spectrum consisting of the sum of spectra c and d [16].

An example of pulse height spectrum of NE213 liquid scintillator measured and calculated for 46 MeV neutrons is shown in Fig. 1.9. Components due to charged products of n-C interactions contribute to this response function in the region to the left of the dashed line ($h < 130$), where the disagreement between calculated and measured responses is very apparent. However, agreement is good in the upper region of the response function ($h \geq 130$) which is due to n-p elastic scattering only.

The different events which arise due to the interaction between the incident radiation (neutron and

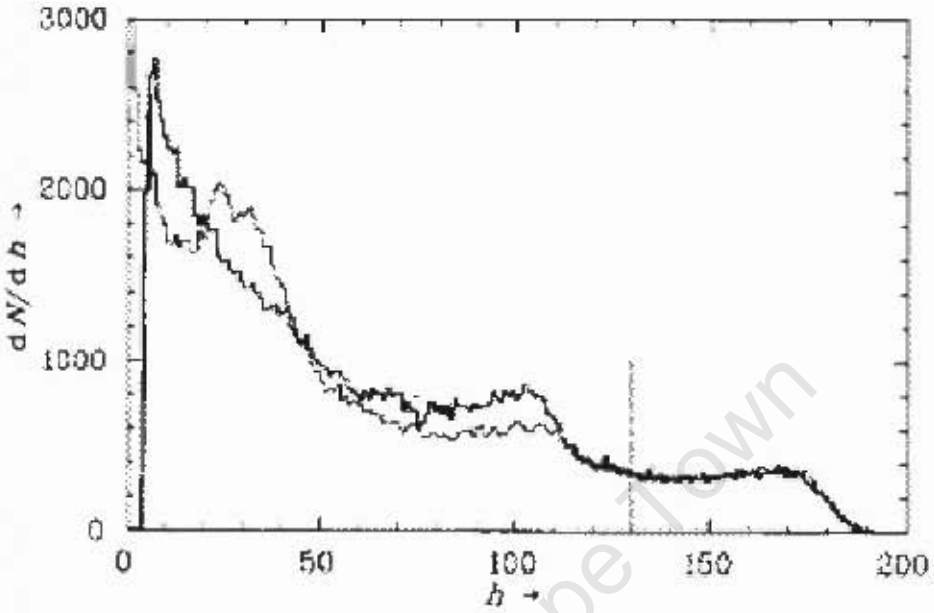

Figure 1.9: Response functions measured with a NE213 liquid scintillator (thick line) and calculated using the code SCINFUL (thin line) for 46 MeV neutrons where dN/dh is the number of counts per pulse height interval as a function of pulse-height (h) [12].

photon) and components of the detector medium, are usually separated by using two-dimensional graphical plots of slow and total component pulse-heights as shown in Fig. 1.10, where p, d, and α are the proton, deuteron and alpha particle produced by neutrons, respectively and e is the electrons produced by photons [30].

1.2.2 Time-of-Flight (TOF)

The Time-of-Flight (TOF) is a technique based on a relationship between the time flight path, t (nano-second) and the kinetic energy of the neutrons, $E_n(MeV)$. The neutrons travel along a flight path, d (meters), towards the detector. The energy of the neutron is measured by taking the time difference between the production point of the neutron (impinging particle on the neutron target) and the subsequent detection of the neutron at the detector located at a given flight path distance. TOF can be calculated using the non-relativistic neutron time of flight equation

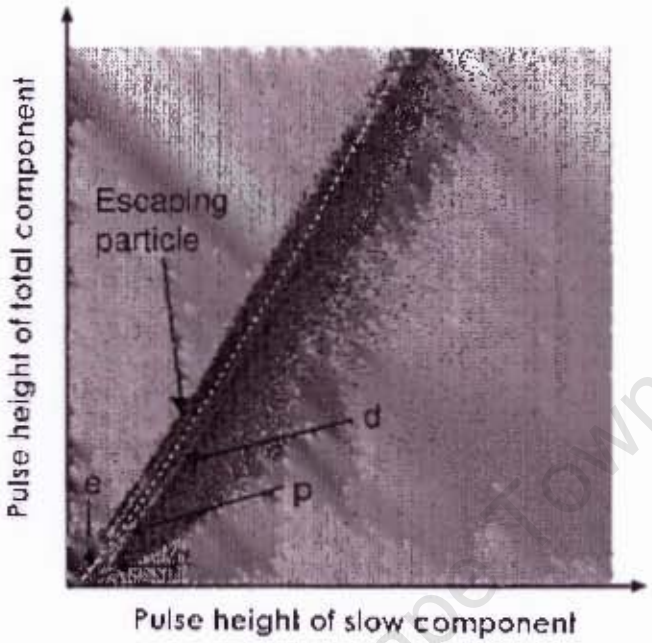

Figure 1.10: Two-dimensional pulse height scatter plots of the slow component versus total component to identify the particles produced in the NE213 scintillator. The discrimination boundary is indicated by the broken line. The symbol e is the electron produced by photons and p, d, and α, are the proton, deuteron and alpha particle produced by neutrons, respectively [30].

$$E_n = \left[\frac{72.3d}{t}\right]^2, \tag{1.3}$$

where

E_n: neutron energy in MeV;

d: Flight path of the neutrons in m;

t: Neutron flight time of the most energetic neutrons in ns; and

72.3: scaling factor.

A typical TOF spectrum obtained from the measurement done by M. Herbert [31] is shown in Fig. 1.11. The spectrum was measured in ADC channels (T) for proton and heavier charged particle events, when exposed to neutrons produced by 66 MeV protons incident on a 1 mm thick ^{7}Li target.

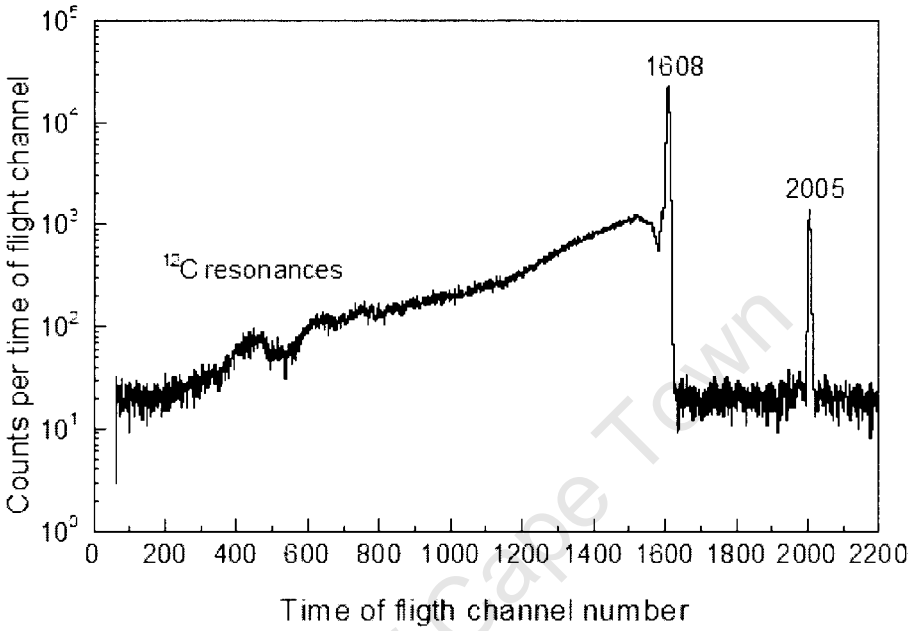

Figure 1.11: TOF spectrum for proton and heavier charged particle events, when exposed to neutrons produced by 66 MeV protons incident on the 1 mm thick ^{7}Li target [31].

In the spectrum, a sharp peak at channel number 1608 corresponding to the highest energy neutrons of 64 MeV (Q = -1.64 MeV) can be seen clearly. This peak arises principally from the transition to the unresolved ground and first excited states of ^{7}Be in the ^{7}Li(p, n)^{7}Be reaction. A gamma peak can be seen at channel number 2005 in the figure, and is attributed to gammas produced in, or around, the target in the proton beam line. The rest of the spectrum consists of a broad lower energy tail, which arises from excitation of the higher states in ^{7}Be or from break up reactions leading to three or more particles in the final state. The full width at half maximum of the gamma peak provides a measure of the intrinsic time resolution of the detector system.

1.3 Previous work

At energy below 20 MeV, measurements of neutron fluence spectra are well established and documented because the relevant cross sections are relatively well known, while above this energy the contribution of the multiparticle break-up from the neutron reaction on the carbon (C)

increases which becomes increasingly difficult to estimate these contributions because the cross-section data that are required are either not available or not accurate enough [32]. Fig. 1.12 shows the total cross sections for n-p interactions and n-C interaction for neutron energies (a) from 0 to 20 MeV [33] and (b) from 20 to 72 MeV [34]. Neutron fluence spectra were measured

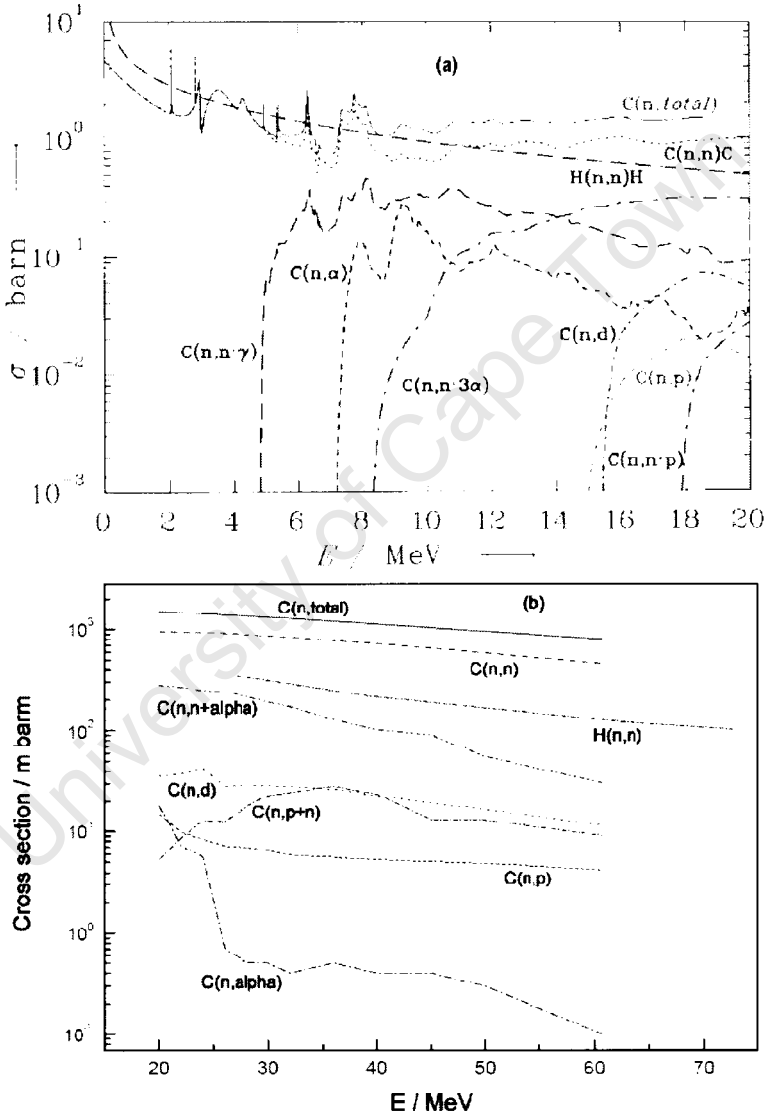

Figure 1.12: Cross sections of various interaction processes of neutrons with carbon nuclei as a function of neutron energy, the n-p scattering cross section is also given for neutron energy range of (a) from 0 up to 20 MeV [33] and (b) from 20 up to 72 MeV [34].

at iThemba LABS at neutron energies up to 150 MeV by Brooks *et al.* [35] by using two different methods: TOF (histogram) and unfolding (points) methods [36]. Fig 1.13 shows the

spectra obtained using (a) Li and (b) graphite targets respectively. In each case, the neutron fluence spectrum shows the high energy peak and continuum neutron spectrum. Also, the fluence spectra obtained by the two methods are in good agreement. A comparison of the measured with

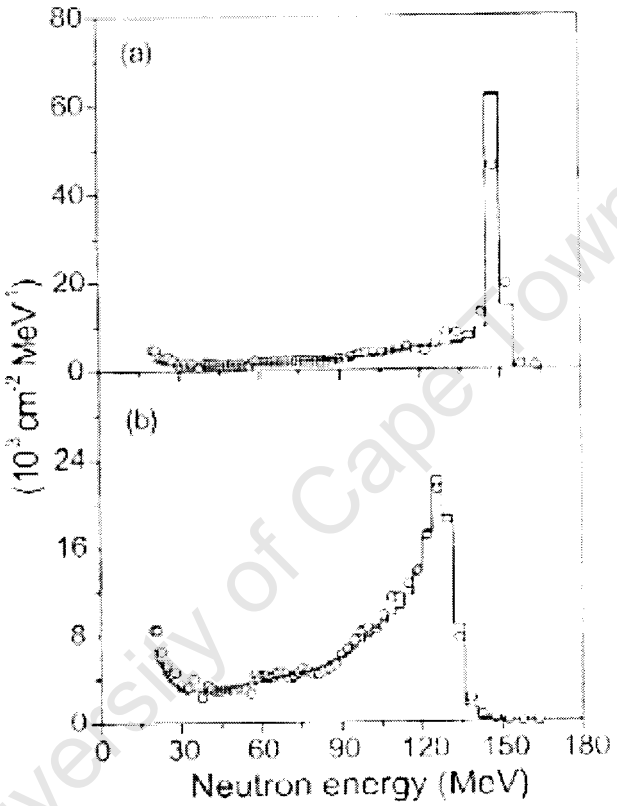

Figure 1.13: Measured neutron fluence spectra obtained from (a) Li target and (b) graphite target, using TOF (histogram) and unfolding (points) methods [35].

the calculated neutron fluence spectrum indicates a good agreement over a wide energy range [9].

Neutron beams measured at 0° and 16° neutron emission angles presented in Fig. 1.3 [5] are characterized by a high energy peak and the continuum extending to low-energy (tail). A proton recoil telescope and NE213 scintillator were used to measure the neutron fluence within the high-energy peak, while a Bonner sphere spectrometer is well suited for the low-energy tail. The aim of this measurement was to come out with a new method which minimizes the contribution from the low energy neutrons to the neutron fluence spectrum. This has been done by subtracting the neutron fluence measured at 16° from the one obtained at 0°. Although this method reduced

the correction of low-energy contribution, the background neutrons are still contributing to the spectrum.

1.4 Present work

The purpose of the study was to investigate the contribution of secondary neutrons produced from interactions of the primary beam with the structural parts aiming to improve and optimize the entire neutron facility at iThemba LABS. More attention is given to the effect of the design of the facility (geometrical and material point of view) on the neutron fluence spectra obtained at various incident proton energies (66, 100 and 200 MeV). This is done by utilizing Monte Carlo based radiation transport codes where the results obtained from the calculations are compared to those obtained experimentally.

The outline of this thesis is as follows: Chapter 2 gives an overview of the FLUKA Monte Carlo radiation transport code as a tool used in this work. Chapter 3 gives a summary of the analysis procedure of the experimental data obtained from the NE213 scintillation detector. In Chapter 4 results obtained from the calculations and are discussed and where available, the calculated data is compared with measured data.

1.5 Monte Carlo simulation codes

Monte Carlo simulations are calculations involving realistic simulations of modelled physical systems and are used in many areas of physics but are of particular importance in the modelling of radiation transport. Particles are created according to rules which determine their type, energy and initial direction. Their interactions with electrons and nuclei within the material of interest are followed according to probabilistic functions using random numbers, which allow the complete history of a particle to be followed as it loses energy within a simulated medium, perhaps generate other particles and ultimately is killed as it either escapes from the geometry of interest or its energy falls below the given threshold.

The problem of simulating the interaction of radiation with matter has a long history, spanning

decades, of applications in physics, medicine and engineering. Two approaches have been developed for this purpose, namely, Monte Carlo and Deterministic Methods [37]. Deterministic Methods are linked to the integro-differential Boltzmann equation, which describes the radiation transport process. This is a discretized process where the resulting system of algebraic equations is solved. Deterministic Methods require reasonably simple geometries for the numerical technique to work, and use the multigroup approximation to cross section data. Monte Carlo techniques are linked to the physics of radiation transport, in which the random history of individual particles is simulated and the results are averaged over many particles. Most Monte Carlo codes can handle complex geometry, continuous as well as multigroup cross section data.

Monte Carlo Methods are stochastic techniques, meaning they are based on the use of random numbers and statistical probability to investigate a variety of mathematical problems, providing approximate solutions to these problems by performing statistical sampling experiments on a computer. If one could determine the exact path each radiation particle makes and its energy, assuming it passes through a medium in a random walk fashion, one could, in principle, simulate a large number of individual particle histories so as to minimize the stochastic effects of the individual particle interactions. For example, the probability that a particle in a certain energy range will be absorbed in a certain volume could be estimated by computing the proportion of all particles in the specific energy group. This concept of using a large number of randomly-generated particle histories to estimate some average particle behavior is an essential feature of Monte Carlo Methods.

The particle tracks (histories) are generated by simulating the random nature of the particle interacting with the medium. This requires mathematical expressions for the probability relationship, which governs the track-length of an individual particle between the points of interaction. The choice of a new energy and new direction, if the interaction is one of a scattering type, and the possible production of additional particles is random; therefore, all the variables are stochastic i.e the solution of these types of problems is based on selecting random numbers.

In order to make selections of the specific values for these variables, one needs a complete understanding of the physics of the various processes a particle undergoes in its lifetime, i.e. from the time it is created in the source until it is absorbed or leaves the system under consideration. In other words, the expected characteristics of particles are estimated by a large number of sampling

of individual particle histories whose trajectories are simulated by a computer. In some cases, there are equations that adequately describe the behavior of such systems and that can be solved either analytically or numerically. The algorithm used for estimating the probability in Monte Carlo codes is described below.

Assume that N particle histories are generated and that n of the histories terminate in the escape of the particle from the system, then to calculate an estimate for the probability that any single particle escapes, a *score*, S_i, is assigned to each particle i as follows: $S_i = 0$ if the particle is absorbed within the system and $S_i = 1$ if the particle escapes. The estimated probability of the escape is given by the mean score:

$$\overline{S} = \frac{1}{N}\sum_i S_i = \frac{n}{N}. \tag{1.4}$$

The relative error (relative statistical uncertainty) indicates the precision of the estimator (tally), not its accuracy. Relative error in that probability estimate is related to the variance S_i, Var(S_i), which can be approximated when N is large

$$\mathrm{Var}(S_i) \approx \frac{1}{N}\sum_i S_i^2 \quad \left(\frac{1}{N}\sum_i S_i\right)^2 = \frac{n(N-n)}{N^2}. \tag{1.5}$$

Then the relative error in the probability estimate is given by

$$\frac{1}{\overline{S}}\sqrt{\frac{\mathrm{Var}(S_i)}{N}} \quad \sqrt{\frac{(N-n)}{Nn}}. \tag{1.6}$$

The general characteristics of a typical Monte Carlo radiation transport codes are:

- Source
- Boundary crossing and geometry
- Distance to collision
- Collision analysis
- Scoring (to estimate or calculate specific quantity)
- Estimate of variance condense intervals
- Variance reduction techniques

Several codes based on Monte Carlo Methods, have been used to model neutron facilities. These include codes such as Monte Carlo N-Particle Transport Code (MCNPX), GEometry ANd Tracking (GEANT4), and FLUktuierende KAscade (FLUKA). MCNPX is a general purpose Monte Carlo radiation transport code that is capable of tracking nearly all particles at nearly all energies. This computer code can treat arbitrary three-dimensional geometries of materials in cells, and uses point-wise (continuous) cross section data with different energy intervals. Fluence, energy deposition, particle pulse height or detectors are examples of the characteristics that can be estimated using this code [38, 39], but this code is not freely distributed due to security reasons.

GEANT4 is an object-oriented Monte-Carlo particle physics simulation toolkit based entirely on the C++ language. Its development started in 1993 in a worldwide collaboration effort RD44 [40]. It is an open source project with updates released usually twice a year available on the official website [41] of the project. This code is more suitable for individual particle tracking but in the case of the energy deposition studies like radiation shielding and dosimetry, where very high statistics for particle transport are needed a code such as FLUKA can be used.

FLUKA is used for a vast variety of applications like proton and electron accelerator shielding applications, target design, calorimetry, activation, dosimetry, detector design, Accelerator Driven Systems, space radiation and cosmic ray showers, neutrino physics and radiotherapy. Particles can be transported in arbitrary complex geometries, details about this code and its uses are given in Chapter 2.

In order to do such simulations of the neutron facility, it is important to understand the basic concepts of the neutron detection as well as the neutron fluence spectra.

Chapter 2

Monte Carlo calculations by means of the FLUKA code

2.1 Introduction to FLUKA code

The FLUKA code was developed in 1962 by J. Ranft and H. Geibel for hadron beams. The name FLUKA (of German origin meaning FLUktuierende KAscade) came eight years later. Since then, the code has been continuously modified and improved to use better and more accurate physical models [42, 43], in order to transport particles from very low energy ranges (thermal) up to very high energies (TeV) for various scientific purposes. The modern code is a multi-purpose Monte Carlo radiation transport code, which, since 1989 has been managed by the collaboration between the Italian National Institute for Nuclear Physics (INFN) and the European Laboratory for Nuclear Particle Physics (CERN). It is used in many fields of physics, both for fundamental research and multi-disciplinary applications.

One of the major advantages of FLUKA compared to other Monte Carlo transport codes is the ability to simulate, with accuracy, the transport of 60 different particles including hadrons, muons, electrons, photons, and low-energy neutrons in a single run without interfacing different codes. Secondary particles produced from the same primary particle are transported before a new primary particle is tracked.

The FLUKA input file is Fortran-based and it consists of fixed-format data cards for numerical parameters. These cards contain information regarding the particle of interest, its energy and position, the geometry of the problem, materials and the estimators (tallies). FLUKA uses a combinatorial geometry package originally developed at ORNL (Oak Ridge National Laboratory) for the neutron and γ-ray transport program MORSE [42, 44]. The package includes additional geometry features, e.g. infinite cylinders, planes and complex geometries. The geometry of the problem is built in three dimensional using a number of standard bodies, e.g. planes, cylinders, spheres, parallelepipeds, etc. defined in regions composed of some materials. Approximately 27 of the well known materials are already predefined in FLUKA.

In FLUKA the primary particle is tracked through its path across the geometry where it propagates unchanged (first free path) until it crosses a boundary to an adjacent region, where it interacts with materials in that region. Depending on the particle and its initial energy, the particle can either interact with the material or can be stopped inside the material (attenuated) if its energy falls below the threshold or it may escape. If an inelastic reaction occurs, secondary particles are produced and tracked. The tracking of particles across boundaries is treated using an improved multiple scattering model derived from Moliere's theory [42]. This model contains a sophisticated algorithm that calculates the distance to the nearest boundary, which allows exact transport of particles across region boundaries. Therefore, boundary crossing points are precisely identified, even in the presence of very thin layers.

The calculation (scoring / estimation / tallying) in FLUKA is carried out in intervals (binnings) depending on the geometry while the yields are obtained by means of an estimator [42]. Various estimators are available to calculate

- Particle fluence and current,
- Number of inelastic reactions in a defined volume,
- Track-length of particles in defined volumes,
- Produced residual nuclei,
- Angle dependent particle production yields,
- Amount of energy deposition in a volume

Particle fluence is calculated using an estimator called USRBDX. In order to calculate the fluence of the particle, relevant information such as the particle of interest, the region for scoring and its dimensions (cm), energy/momentum range (GeV), angle range (steradian) and number of histories/cascades is needed. In FLUKA the particle fluence, ϕ, is calculated using the following equation

$$\phi = \frac{\text{number of particles}}{E \times A \times pr}, \tag{2.1}$$

where E is the particle energy (GeV), pr is number of primary particles (histories) and A is the boundary area (cm^2).

Neutron interactions are treated by means of different hadronic interaction models, depending on the initial energy of the primary particles. A full description of these models and their most recent developments can be found in [45, 46]. Neutrons with energies below 20 MeV (low energy neutrons) are treated separately from those with energies above 20 MeV (high energy neutrons).

High energy neutrons are treated by means of a hadronic model called the Pre-Equilibrium Approach to NuclearThermalization (PEANUT) [47]. This model describes the hadronic interactions using a very detailed Generalised Intra-Nuclear Cascade (INC)[1] and pre-equilibrium stage models [48, 49, 50], followed by equilibrium processes: evaporation, fission, Fermi break-up and gamma de-excitation.

Low energy neutrons are modeled by means of a multi-group algorithm known as the Legendre angular expansion, which uses cross sections obtained from standard evaluated data, consisting of 72 neutron energy groups e.g. ENDFB-VI, JEFF, JENDL, etc. and equipped with standard processing tools [51, 52]. In this multi-group algorithm, the particle energy range is divided into intervals (energy groups) while elastic and inelastic scattering reactions are simulated by group-to-group ($g \longrightarrow g^{'}$) transfer probabilities. The scattering transfer probability, P_i, between different groups is represented by a P5 Legendre angular expansion

$$\sigma_s(g \longrightarrow g^{'}, \mu) = \sum_{i=0}^{N} \frac{2i+1}{4\pi} P_i(\mu) \sigma_s^i(g \longrightarrow g^{'}), \tag{2.2}$$

where σ_s and μ are the scattering cross section and angle, respectively. This model contains detailed kinematics of elastic scattering on hydrogen nuclei, which includes the transport of

[1]INC: Is a mechanism in which hadron-nucleus (h-A) reactions are described as a cascade of two-body interactions, concerning the projectile and the reaction products at energies high enough to consider coherent effects as corrections.

proton recoils. However, photons emitted after an inelastic reaction or neutron capture are not treated in accordance with the multi-group algorithm but they are treated using a more accurate Electro-Magnetic FLUKA (EMF) package, which performs continuous transport with respect to energy [53, 54]. The electromagnetic sector is fully coupled to the hadronic one, e.g. photons from nuclear de-excitation are directly transported by EMF [52, 55]. For nuclei other than hydrogen, kerma factor is used to calculate the energy deposition, while electrons are transported by the EMF package [56, 57].

An example of a generalized FLUKA input file is given below. The particle source (beam) is described by the BEAM and BEAMPOS cards, while the geometry of the problem is described inside GEOBEGIN and GEOEND and materials are assigned according to the geometrical regions in the ASSIGNMAT card. The EMFCUT card denotes the energy cut-off for the production of electrons, positrons and photons when the primary particle interacts with some material. The default maximum energy threshold is 10 MeV. The SCORE card, defines the particles producing stars (hadronic inelastic interaction, which occurs at an energy higher than the threshold energy of the selected particle) and it is responsible for the energy deposition in each region. As mentioned above USRBDX is used to estimate the fluence or current and it can be given as a differential fluence (energy dependent) or as a double differential fluence (energy and angle dependent).

An Example of FLUKA input file is shown in the frame below.

```
TITLE
*
BEAM            Kinetic Energy / Momentum                                    PROTON
BEAMPOS          X-coordinate     Y-coordinate     Z-coordinate
GEOBEGIN                                                                     COMBNAME
                        A simple Be target inside Air
RPP body1   Xmin      Xmax          Ymin     Ymax          Zmin     Zmax
RPP body2   Xmin      Xmax          Ymin     Ymax          Zmin     Zmax
RPP body3   Xmin      Xmax          Ymin     Ymax          Zmin     Zmax
RPP body4   Xmin      Xmax          Ymin     Ymax          Zmin     Zmax
RPP body5   Xmin      Xmax          Ymin     Ymax          Zmin     Zmax
*RPP: Rectangular parallelepiped
*has minimum and maximum coordinates bound the parallelepiped
END
*
regBH1    5     +body1 -body2
regVA2    5     +body2 -body3
regAi3    5     +body3 -body4
regAi4    5     +body4 -body5
regFe5    5     +body5
END
GEOEND
*
MATERIAL                      density in $g/cm^2$   material number            material name
COMPOUND  mass fraction of mat1  mat1 number  mass fraction mat2  mat2 number   compound name
ASSIGNMAT   BLCKHOLE  regBH1
ASSIGNMAT   VACUUM    regVA2
ASSIGNMAT   AIR       regAi3
ASSIGNMAT   AIR       regAi4
ASSIGNMAT   IRON      regFe5
*
SCORE       ENERGY    BEAMPART
* Boundary crossing fluence in the middle of the target (log intervals, one-way)
*
USRBDX one-way fluence  particle type  output unit  regAi4  regAi3  detector area  pFluenUD
USRBDX maximum kinetic energy  energy interval number  maximum solid angle  angular bins number &
*
RANDOMIZE    logical file unit from which to read the seeds
*
START       maximum number of primary histories simulated in the run
STOP
```

2.2 Simulations of the neutron experimental facility

The main aim of the present study is to simulate the neutron facility at iThemba LABS [1] in order to investigate the secondary neutron background. Since the details of the facility were discussed in Chapter 1, here we limit our discussion to the simulations.

At iThemba LABS neutrons are produced by bombarding either a ^{7}Li, ^{9}Be, or ^{12}C target with a beam of protons of energy up to 200 MeV. A schematic depiction of the neutron facility as it was modelled is shown in Fig. 1.2. This experimental facility was simulated using FLUKA, version 2006.3b. The aim of the calculation was to investigate whether the collimation system and/or shielding need modifications, with an aim to improve the facility for experimental purposes.

2.2.1 The Monte Carlo model structure of the present problem

When a fast neutron beam enters the geometry it interacts with different materials (air, iron, concrete, etc.) inside the region. Each possible interaction has a certain probability (cross section). A Monte Carlo program that solves the behavior of this system could, therefore, be described in the following way:

- A primary neutron with energy (E_n) and at position (x, y, z) with respect to the geometry, interacts with the material inside the regions of interest,
- This neutron, and all subsequently produced neutrons (secondaries) are transported. The coordinates of the neutron will remain unchanged when traversing / passing through a given geometry until an interaction occurs, in which case the particle's direction is changed,
- The track length is determined by the probability of the neutron to interact, its energy and position in the current medium,
- Possible interaction cross sections for the neutron are taken into account by means of an algorithm based on the Legendre polynomial expansion,
- If the neutron leaves the reaction point, its energy and scattering angle will be assigned,

- The neutron is subsequently tracked until it undergoes a scattering interaction (elastic or inelastic) where it is either transformed, absorbed, or leaves the region of interest,
- The neutron fluence, is then calculated, per region of interest, as a function of energy (differential) or by also integrating over the solid angle and energy (double differential).

A flow chart that describes the history of the neutron from initialization to interaction with materials until it is terminated is given in the context of FLUKA in Fig. 2.1. The study of the neutron background in the facility was performed in a series of steps described below.

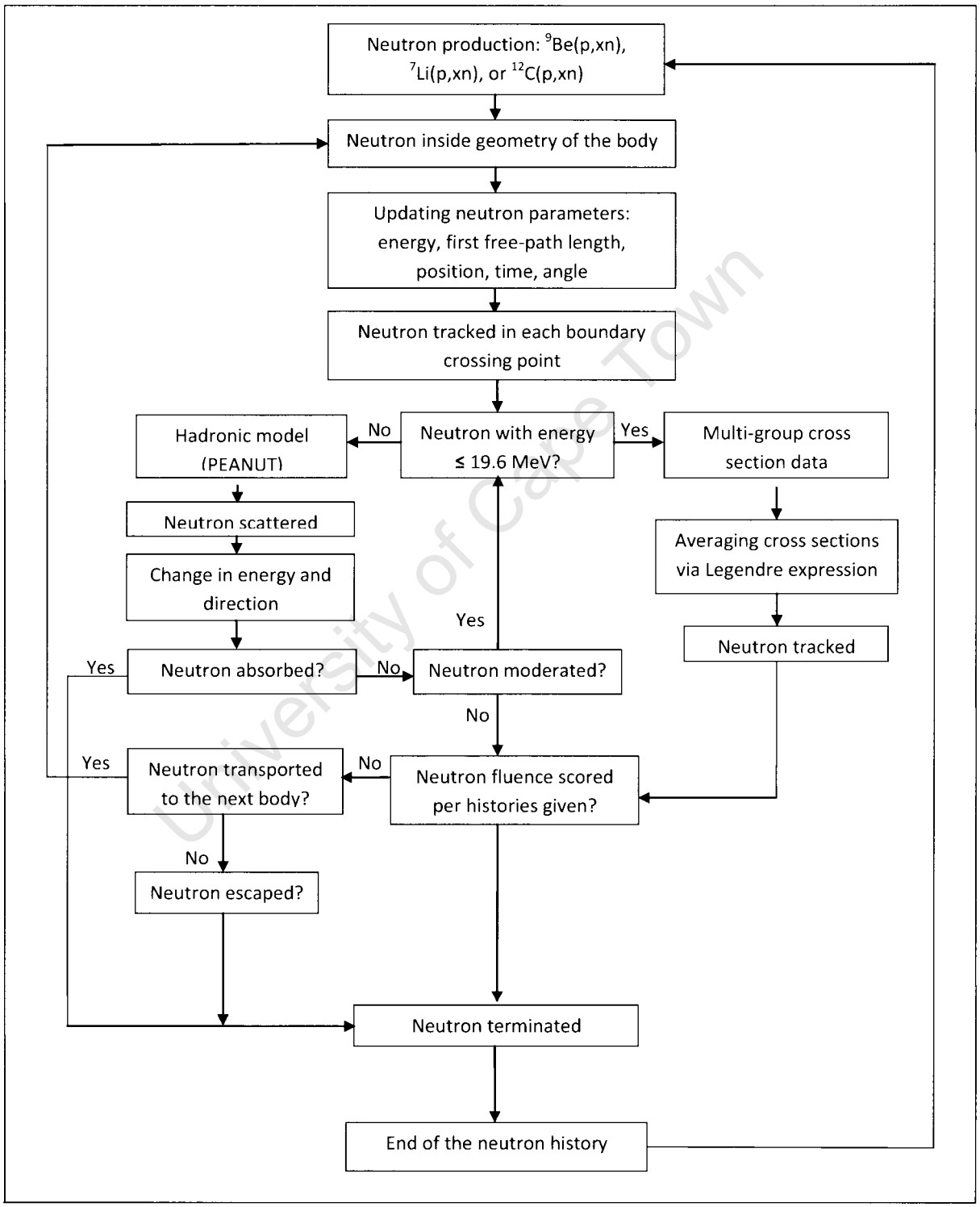

Figure 2.1: Flowchart describing the neutron history tracked by FLUKA in a defined body.

2.2.2 Beam profile

This study was done in order to ascertain a suitable beam for the production of the neutron at iThemba LABS. Three types of proton beams were investigated in this study: pencil, halo, and diverging beams. For this simulation we considered a 200 MeV proton beam incident on a 10 mm thick ^{9}Be target and a 5 cm diameter detector placed at a distance of 7.7 m away from the target at 0 degree neutron emission angle with respect to the beam axis. For the pencil beam, information about the kinetic energy of the particle and its weight (1.0) is needed. The pencil beam was simulated using information given in the card below.

```
BEAM          kinetic energy          beam weight          Proton
```

In contrast, the halo beam requires additional information such as inner radius (0.7 cm) and the outer radius (1.2 cm) as shown below.

```
BEAM    kinetic energy    outer radius    inner radius    beam weight    Proton
```

The last test involved simulating a beam diverging at 3 mrad in the x-direction (particle beam direction).

```
BEAM        kinetic energy        divergence value        beam weight        Proton
```


2.2.3 Neutron emission angle

This section describes tests carried out to study the effect of neutron emission angle on the neutron energy spectrum. Simulations were done to calculate the fluence of neutrons produced in the irradiation of a 10 mm thick ^{9}Be target with 200 MeV protons, at a distance of 7.7 m and emission angles of 0, 4, 8 and 16 degrees with respect to the beam axis. The geometry describing this scenario is shown in Fig. 2.2.

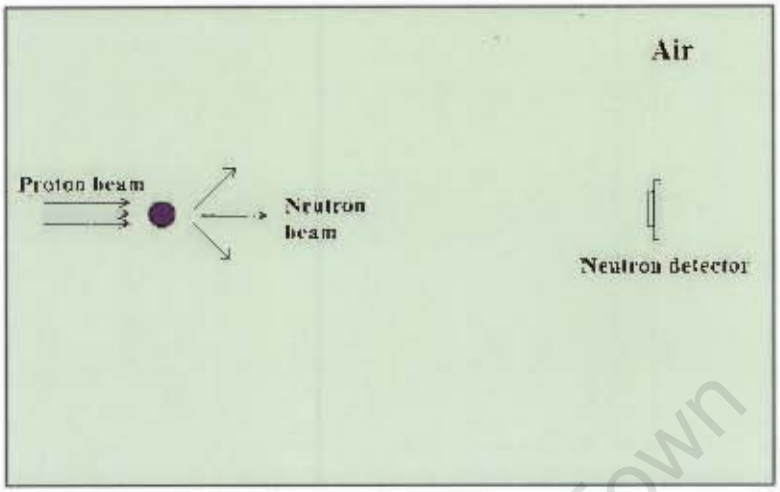

Figure 2.2: Schematic depiction of the detector with respect to the neutron source.

2.2.4 Production of neutrons from different targets

Neutron beams of energies up to 200 MeV were produced from the interaction of protons with different targets (^{7}Li, ^{9}Be, and ^{12}C) which are available at iThemba LABS. Each target is dominate in specific region with in this energy range (0 - 200 MeV), i.e. the neutron spectrum for ^{7}Li covers the high energy region and the spectrum for ^{9}Be covers the medium region while the spectrum for ^{12}C covers low energy region with in the given energy range. In order to investigate the effect of target thickness on the neutron fluence spectrum and to understand how the production of the neutron vary with target thickness, three different thicknesses 3, 5 and 10 mm for each target were used. Each target interacted with protons of energies of 66 MeV, 100 MeV and 200 MeV protons at position 0 0 0 cm with respect to the beam axis, and a 5 cm diameter detector situated at 7.7 m away from the target was used. The neutron fluence were then calculated as a function of neutron energy at 0 degrees emission angle.

2.2.5 Study of the neutron background

The simulations were performed in order to investigate the neutron background in the experimental area. This was done in several stages described below.

A 200 MeV proton beam with a halo of inner and outer radii of 0.7 and 1.2 cm, respectively,

impinging on a 10 mm thick ^{9}Be target was simulated. The target was placed on a ladder composed of a 50 μm havar foil at position 0 0 0 with respect to the room 200 $cm \times 300$ $cm \times$ 1300 cm filled with air. The neutron fluence was calculated at a distance of 7.7 m and at emission angle of 0 degree with respect to the beam axis.

A collimator, used to focus the neutron beam, was then introduced into the geometry at 200 cm away from the target at position 0 0 200 cm with respect to the room axis. This collimator was about 3 m long, with a 2.5 cm circular opening. As shown in Fig. 2.3, the collimator was surrounded by a radiation shield composed of concrete, iron and borated polyethylene materials of different thicknesses. The neutron fluence was also calculated.

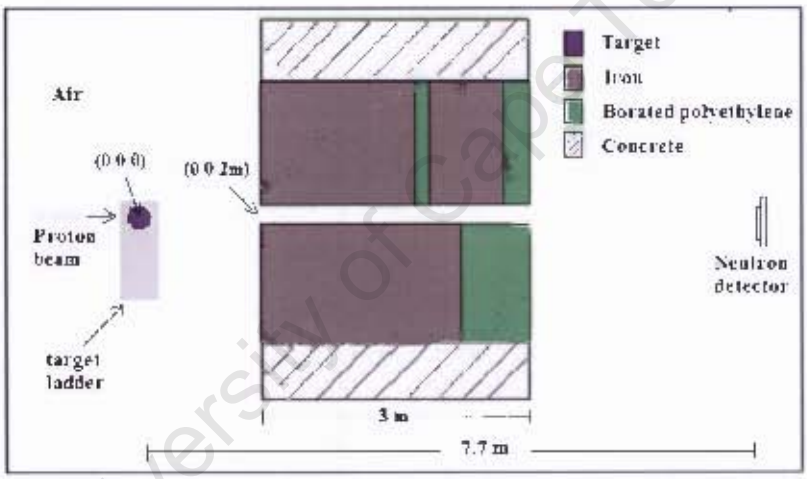

Figure 2.3: Layout of the collimator system

The clearing magnet, beam dump, graphite block, concrete wall and outer parts of the collimator, e.g. emission angle openings (4, 8 and 16 degrees), were also introduced into the geometry. A 5 cm thick clearing magnet was introduced in the neutron beam line at a distance of $\approx$ 50 cm a way from the target to attracts the charged particles that did not interact with the target and steers them into the 165 cm long beam dump composed of a mixture of carbon and copper materials. The 5 cm x 5 cm graphite was inserted inside the collimator and the 2 m thick concrete was introduced around the collimator as shown in Fig. 1.2. The neutron fluence was also obtained. Also, in order to compare with the available experimental results, neutron fluence were calculated for the 66 MeV protons on a 1 mm ^{7}Li, 10 mm ^{9}Be and 10 mm ^{12}C targets.

The last part of the simulations entailed modeling neutron fluence at specific positions in front

of the borated polyethylene door as well as in front of the collimator body. The ^{9}Be(p,n)^{9}B reaction was used. The neutron detector was then introduced at distances of 50 and 250 cm from the borated polyethylene door (positions p1 and p2 in Fig. 1.2 which corresponds to angles of 31 and 19 degrees with respect to the beam axis) and at distances of 1 and 150 cm from the shielding wall (positions p3 and p4 corresponding to angles of 23 and 12 degrees). The results were compared with those obtained at 0 degrees and at 7.7 m from the target (position p5). The results obtained in this study are presented in Chapter 4. One of the input files used for the calculation and the values of the fluence obtained from this input file are given in Appendix A.

Chapter 3

Analysis of neutron fluence from measured data

3.1 Overview of the measurement

The experimental data presented in this work was obtained from the measurements carried out in the neutron facility at iThemba LABS [1] by M. Herbert $et\ al.$ [31, 58] (for more details on the facility see Chapter 1). A brief overview of the data reduction techniques to extract neutron fluence spectra from the measured pulse height and time-of-flight spectra will be presented in this chapter and appendix B. In this experiment, a 66 MeV proton beam from iThemba LABS, separated sector cyclotron was used to irradiate three different targets to produce neutron beams. The targets used were Lithium metal (^{7}Li), Beryllium metal (^{9}Be) and Carbon (^{12}C) of thickness of 1 mm, 10 mm and 10 mm, respectively.

Measurements were carried out using a cylindrical NE213 organic liquid scintillator of 50 mm diameter $\times$ 50 mm placed at a distance of 7.7 m away from the target. A circular collimator aperture of diameter of 25 mm was used to produce a neutron beam at 0° neutron emission angle with respect to the beam axis. The pulse height, L, of the scintillation, the neutron time-of-flight parameter, T_n, and the the fast component of the scintillation pulse, F, were recorded and the data was analyzed off-line. Link pulse shape discrimination unit (model 5010) [18] was used to generate the L and F parameters which were used for particle identification. Reduction of the

data carried out are described below. Details of the software cuts used to select events of interest are presented in Appendix B.

3.2 Neutron fluence spectrum

To obtain a neutron fluence spectrum, the detection efficiency of the detector as a function of the neutron energy is required. In this work the neutron detection efficiency was calculated for a NE213 scintillator detector. In this case the neutron should transfer enough energy to a charged particle for the scintillation pulse to exceed the electronic detection threshold of the detection system. Therefore, the efficiency of the NE213 scintillator detector depends on the energy of the incident neutron, total cross section of the nuclear interaction e.g n-p elastic scattering which is used in neutron detection, geometry of the detector (its shape and size) and the electronic threshold of the detector.

Fig 3.1 shows the pulse height spectrum measured in a NE213 scintillator for mono-energetic neutrons of energy of 64 MeV. Events shown in Fig. 3.1 were selected by imposing software windows (cuts) on the two parameter plots of (i) events versus pulse height and TOF i.e LT plots (see Fig. B.6) and (ii) for time (energy) events versus pulse height and pulse shape parameter i.e LS plots (see Fig. B.4) to select charged particle events. This pulse height was set to select proton events (n-p elastic scattering) induced by the mono-energetic neutrons in the pulse height spectrum above the pulse height threshold L_{np}.

The total number of neutrons N_{np} determined above the pulse height threshold L_{np} is then given by

$$N_{np} = \epsilon_H(E_n, L_{np})N_o = N_o\dot{\varphi}_{npf}(E_n, L_{np})\dot{\varphi}_{npc}(E_n).\sigma_H(E_n)n_H, \tag{3.1}$$

where

$\epsilon_H(E_n, L_{np})$: neutron detection efficiency, see Appendix B for the efficiency disscusion and calculations

E_n: neutron energy;

N_o : the number of neutrons of energy E_n incident on the NE213;

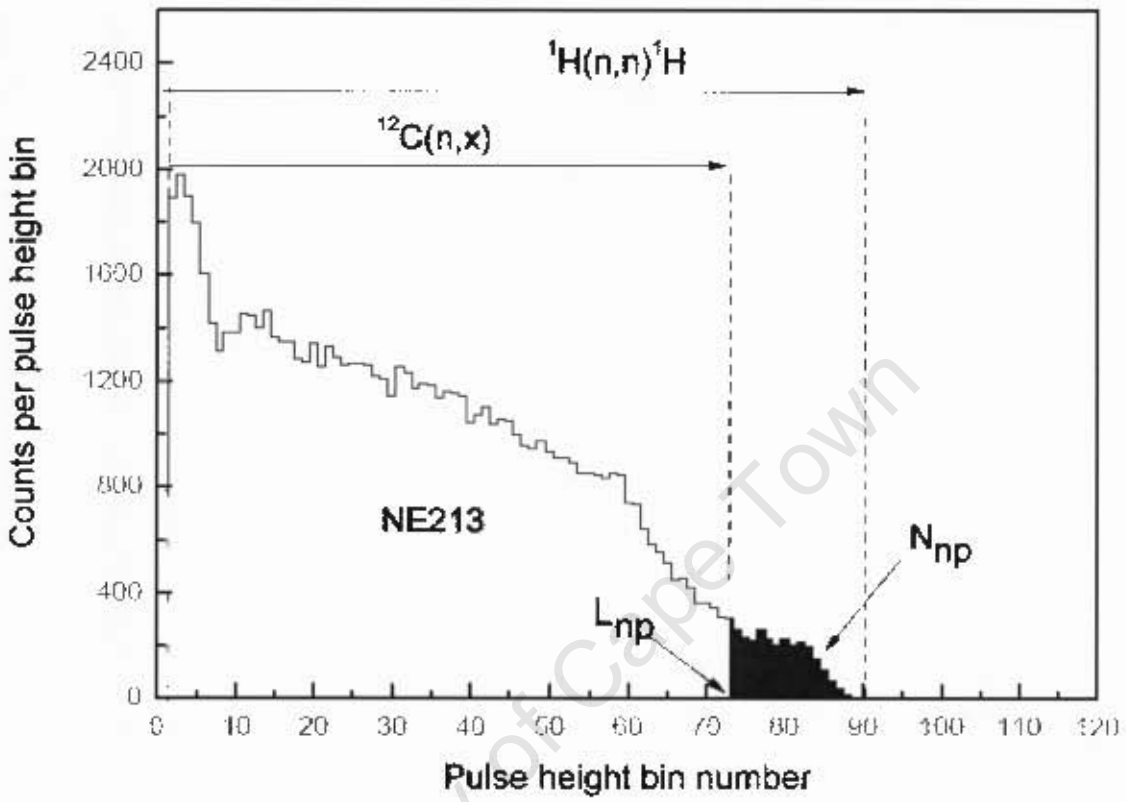

Figure 3.1: Pulse height spectrum measured for neutrons of energy 64 MeV using NE213.

$\sigma_H(E_n)$: the total cross section for n-p elastic scattering.

If the cross sectional area of the beam is A, then the neutron fluence can be given by

$$\Phi = \frac{N_o}{A}. \tag{3.2}$$

Using equation 3.1, the equation for the neutron fluence measurement becomes

$$\Phi = \frac{N_{np}}{A\varepsilon_{npf}(E_n, L_{np})\varepsilon_{npe}(E_n)\sigma_H(E_n)n_H}. \tag{3.3}$$

Each input quantity in equation 3.3 is considered separately and discussion on how each of these quantities was obtained is given below.

(a) N_{np}: the count measured above the pulse height threshold L_{np}: The pulse height threshold used for L_{np} was 73 ADC (pulse height bin number). It was used to select all events of protons recoiling from n-p elastic scattering N_{np}. The integral count of all events above L_{np} was found to be 2915 counts.

(b) σ_H: the total cross section for n-p elastic scattering: The value of the total cross section for the n-p elastic scattering at neutron energy of 64 MeV is 0.123 barn. The total cross section for n-p elastic scattering used in this work obtained from [31] is shown in Fig. 3.2

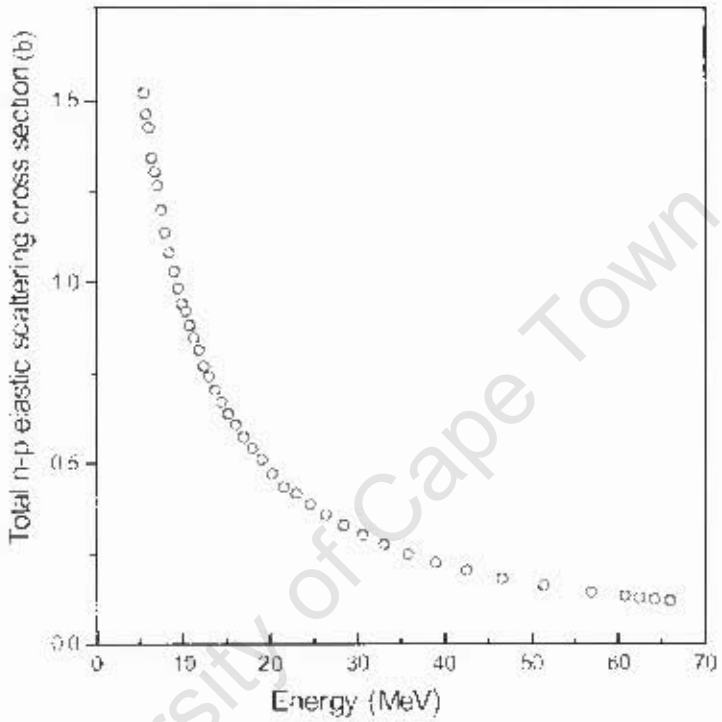

Figure 3.2: Total n-p elastic scattering cross-section as a function of neutron energy [31].

(c) n_H: the number of hydrogen nuclei per unit cross sectional area presented to the neutron beam by the NE213 scintillator: It is given by the equation below.

$$n_H = \frac{N_A \rho x \eta_H}{M}, \tag{3.4}$$

where:

N_A: Avogadro's number $= 6.022 \times 10^{23}$ mol $^{-1}$,

ρ: density of NE213 liquid scintillator = 0.874 g.cm^2,

η_H: number of hydrogen atoms per molecule of NE213 liquid scintillator = 10.2,

x: the length of the NE213 scintillator = 5 cm, and

M: molar mass of NE213 scintillator = 106 g.mol^{-1}

(d) A: cross sectional area of the beam: The radius of the beam at the detector was found to be 2.5 cm therefore, the cross sectional area of the beam was taken to be $\pi \times 2.5 \times 2.5$ cm^2.

(e) ε_{rpe}: correction factor for escaping protons: The range as a function of the neutron energy for protons, deuterons and alpha particles in NE213 organic liquid scintillator can be seen in Fig. 3.3 [59].

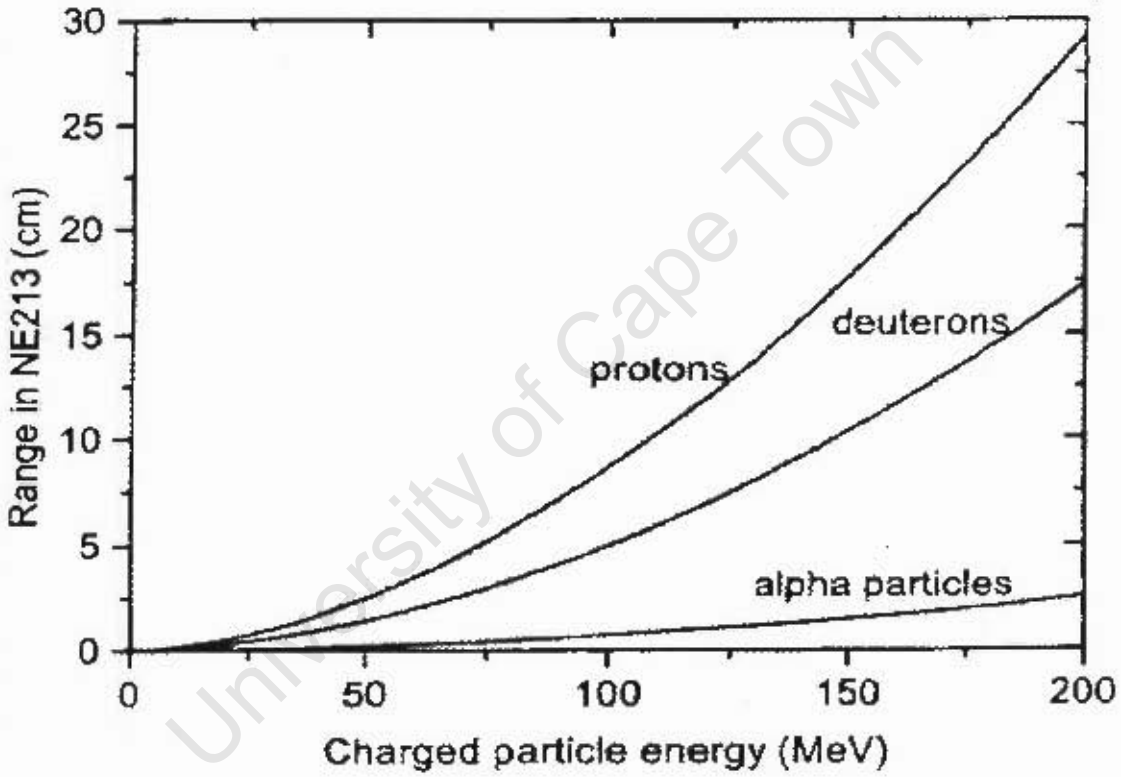

Figure 3.3: The ranges of different charged particles as the function of the neutron energy in NE213 scintillator [59].

By using the equation presented in [60], one can determine the ratio of the total number of protons, which recoil directly forward from n-p elastic scattering events in the NE213 scintillator, to the number of such protons which do not escape from the scintillator as

$$\frac{\text{total proton events}}{\text{proton non escape}} = \frac{\pi r^2}{r^2 \cos^{-1}\left(\frac{s^2}{2r^2} - 1\right) - 0.5\sqrt{4r^2 - s^2}}, \tag{3.5}$$

where r is the radius of the NE213 scintillator and s is the range of a proton in the NE213 scintillator at a particular energy. From Fig. 3.3 the range of 64 MeV protons in NE213 is 3.95

cm. By using this range in equation 3.5, the radius of 2.5 cm of the NE213 and the escape correction factor for recoiling protons, ϕ_{npc} above pulse height threshold L_{np} was calculated to be 0.116.

(f) ϕ_{npf}: the fraction of n-p elastic scattering events detected above the pulse height threshold L_{np}: The recoiling protons from n-p elastic scattering with energy greater than E_{np} = 51.4 MeV lie within a cone, with internal angle, ξ, in the laboratory frame. This angle is related to the incident neutron energy E_n, and the recoiling proton energy E_p by

$$\cos\xi = \frac{E_p}{m_p c^2(\gamma_2 - 1)} - 1, \tag{3.6}$$

with

$$\gamma_2 = \frac{\frac{m_p}{m_n} + \frac{E_n}{m_n c^2}}{\left[\left(\frac{m_p}{m_n}\right)^2 - \frac{2m_p E_n}{(m_n c)^2} + 1\right]^{1/2}}, \tag{3.7}$$

where m_p and m_n are the respective rest masses of the proton and neutron, and c the speed of light. The scattered neutron angle, θ, in the center-of-mass frame is given by

$$\theta = 180 - \xi \tag{3.8}$$

or from equation3.6

$$\cos\theta = 1 - \frac{E_p}{m_p c^2(\gamma_2 - 1)} \tag{3.9}$$

Therefore, E_{np} is related to an associated scattered neutron angle θ_{np} in the center-of-mass frame by

$$\cos\theta_{np} = 1 - \frac{E_{np}}{m_p c^2(\gamma_2 - 1)} \tag{3.10}$$

The fraction of recoiling protons ϕ_{npf} from n-p elastic scattering detected above the recoiling proton threshold energy E_{np} may then be calculated by

$$\phi_{npf} = \frac{\int_{\theta_{np}}^{\pi} \sigma_H(E_n, \theta) d\theta}{\int_0^{\pi} \sigma_H(E_n, \theta) d\theta}. \tag{3.11}$$

Fig. 3.4 shows the differential cross sections for the n-p elastic scattering obtained from ENDF data sets [61]. The figure shows the recommended evaluations as a function of scattered neutron angle in the center of mass system (cos θ), and incident neutron energy in the range 10 to 100 MeV.

By substituting the value of the recoiling proton threshold energy, E_{np} = 51.4 MeV, for E_n = 64 MeV in equation 3.10, $\cos\theta_{np}$ was determined to be -0.608 and θ_{np} = 127.30°. Using θ_{np} =

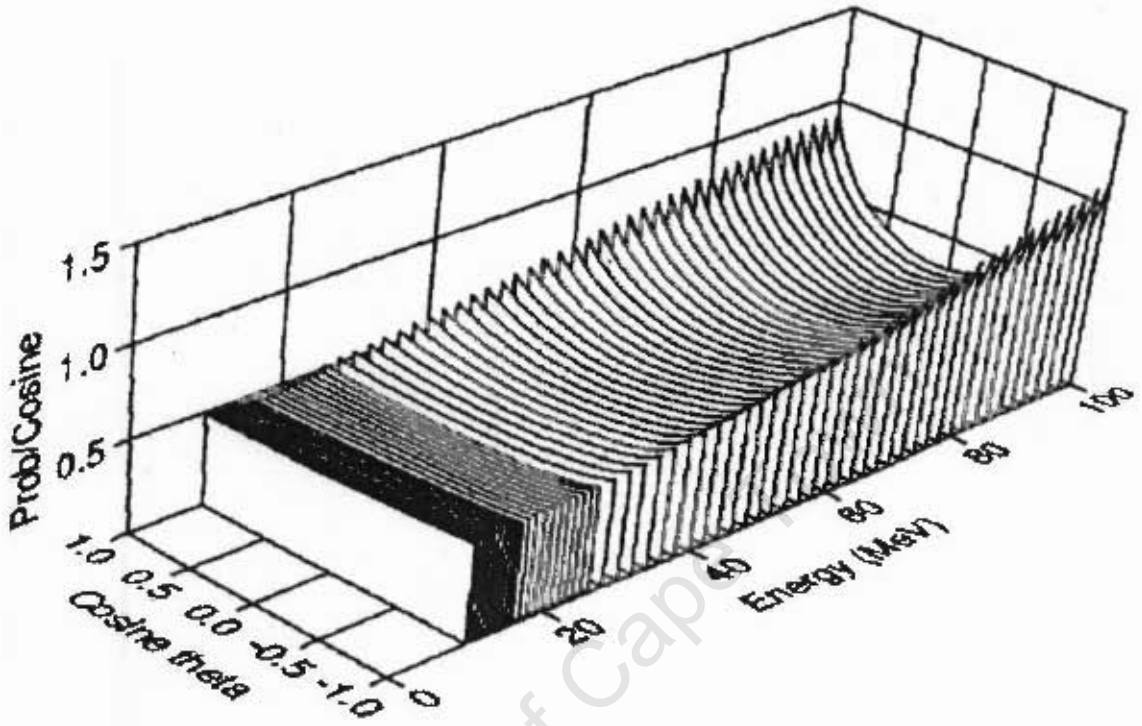

Figure 3.4: Differential cross sections for n-p elastic scattering obtained from the ENDF data [61].

127.30° and data from ENDF shown in fig. 3.4, the value of ϕ_{npf} was found to be 0.255 from equation 3.11.

3.2.1 The uncertainty in neutron fluence u(Φ)

The uncertainty in the neutron fluence entering the NE213 arises from the uncertainty associated with each of the input quantities used in equation 3.3. The uncertainty in N_{np} is calculated by means of statistical methods. Thus, the uncertainty in N_{np} is given by its square root. The uncertainties in $A, n_H, \phi_{npf}, \phi_{npe}$ and σ_H are in these cases a rectangular probability density function used to model the available knowledge about them [62, 63]. The uncertainty $u(x)$ is given by

$$u(x) = \frac{\frac{1}{2}(x_{right} - x_{left})}{\sqrt{3}}, \tag{3.12}$$

and if a triangular probability density function is used, then the uncertainty may be given by

$$u(x) = \frac{\frac{1}{2}(x_{right} - x_{left})}{\sqrt{6}}, \tag{3.13}$$

where x_{right} and x_{left} are the limits of the probability density function. The combined uncertainty in ϕ is then given by

$$\left[\frac{u(\Phi)}{\Phi}\right]^2 \quad \sum_i \left[\frac{u(x_i)}{x_i}\right]^2, \tag{3.14}$$

where x_i and $u(x_i)$ are the best estimates and uncertainties, respectively for each input quantity in equation 3.3. Using equation 3.14, the uncertainty $u(\epsilon)$ in the neutron fluence $u(\Phi)$ was determined, using the best estimates and uncertainties respectively, for each input quantity in equations and 3.3 at each energy. Table 3.1 presents each input quantity used in equation 3.3, with their best estimate for the incident neutron 64 MeV, and it is also shown the right (x_{right}) and left (x_{left}) hand values used for each pdf, this calculation for the ^{7}Li target only. In the same way, uncertainty $u(\Phi)$ in the neutron fluence for ^{9}Be, and ^{12}C were determined .

Table 3.1: Best estimate and uncertainty of each input quantity used in equation 3.3 to determine uncertainty in the neutron fluence of NE213 for the incident neutron 64 MeV.

Input quantity	Best estimate x_i	Uncertainty $u(x_i)$	x_{left}	x_{right}
N_{np}	1905.0	0.0575	-	-
σ_H	0.124	0.003	0.117	0.127
A (cm^2)	32.0	0.1139	31.902	32.198
n_H	0.252	0.010	0.230	0.264
ϕ_{npf}	0.255	0.009	0.23	0.26
ϕ_{nps}	0.116	0.031	0.05	0.16

Table 3.2 shows the factors used to calculate the neutron fluence for each target (^{7}Li, ^{9}Be, and ^{12}C). Table 3.3 shows the values of neutron fluence with their uncertainties as a function of energy bin for the three targets (^{7}Li,^{9}Be and ^{12}C). Using table 3.3 neutron fluence for ^{7}Li, ^{9}Be and ^{12}C targets were plotted with their uncertainties as a function of energy bin and compared with the calculated results are discussed in Chapter 4.

Table 3.2: Factors used to calculate the neutron fluence for ^{7}Li, ^{9}Be, and ^{12}C.

E_n (MeV)	L_{np} channel	n_H (barn^{-1})	σ_H (barn)	θ_{np} (o)	ϕ_{npf}	$u(\phi_{^{12}C})$	$u(\phi_{^{12}C})$ (counts)	$u(\phi_{^{12}C})$ (counts)	$u(\phi_{^{12}C})$ (counts)
5.36	1	0.252	1.551	150	0.081	0.995	64	630	1102
5.63	1	0.252	1.49	140.9	0.122	0.994	226	1613	3516
5.92	1	0.252	1.434	133.6	0.173	0.993	459	3559	7487
6.23	1	0.252	1.381	127.2	0.213	0.993	668	5366	12015
6.56	1	0.252	1.332	121.6	0.254	0.992	1534	12070	28064
6.93	1	0.252	1.271	116.3	0.294	0.991	2295	17407	41111
7.32	1	0.252	1.23	111.5	0.334	0.99	1872	13568	33018
7.75	1	0.252	1.165	106.9	0.37	0.975	1576	12010	28707
8.22	1	0.252	1.107	102.5	0.405	0.974	3006	21320	51154
8.65	1	0.252	1.067	99	0.435	0.973	4266	29315	71850
9.2	1	0.252	1.004	95	0.475	0.971	2807	19299	46771
9.6	1	0.252	0.97	92.4	0.502	0.97	3169	31370	53192
10.03	1	0.252	0.938	89.8	0.514	0.963	3716	24738	60010
10.49	1	0.252	0.899	87.3	0.54	0.961	3616	24274	61264
10.97	1	0.252	0.862	84.9	0.56	0.96	3503	23292	58723
11.5	2	0.252	0.828	82.5	0.579	0.953	3659	23346	59665
12.06	3	0.252	0.796	80.2	0.599	0.951	3357	21192	55288
12.67	4	0.252	0.76	77.8	0.614	0.945	3401	21265	59105
13.32	5	0.252	0.723	75.6	0.634	0.943	3195	20717	50278
14.02	7	0.252	0.689	73.3	0.658	0.937	2982	18936	50764
14.78	8	0.252	0.655	71.1	0.672	0.93	2896	18046	48112
15.61	9	0.252	0.62	68.9	0.692	0.924	2874	17130	46538
16.51	10	0.252	0.587	66.8	0.707	0.913	3093	18119	49608
17.49	12	0.252	0.553	63.9	0.731	0.905	2874	17201	47393
18.56	14	0.252	0.523	69.1	0.692	0.894	2747	4741	44365
19.73	15	0.252	0.489	74	0.653	0.882	2911	5095	46774
21.02	17	0.252	0.458	78.6	0.614	0.867	3085	4234	48649
22.43	18	0.252	0.426	83	0.574	0.85	3612	5399	55202
24	22	0.252	0.397	87.2	0.54	0.832	3111	17155	46361
25.75	24	0.252	0.368	91.3	0.504	0.808	3419	18055	49377
27.69	27	0.252	0.337	95.2	0.47	0.782	3380	17547	46780
29.87	31	0.252	0.307	99	0.437	0.75	3206	15409	42340
32.31	35	0.252	0.281	102.8	0.409	0.712	2866	13864	36878
35.08	38	0.252	0.255	106.4	0.382	0.667	2955	14065	34835
38.23	42	0.252	0.23	110	0.355	0.613	2830	12752	28119
41.83	46	0.252	0.206	113.5	0.329	0.547	2819	12658	17371
45.97	53	0.252	0.184	116.9	0.309	0.468	2211	15751	7230
50.78	59	0.252	0.163	120.3	0.286	0.373	1653	21954	527
56.42	65	0.252	0.144	123.6	0.274	0.26	926	19126	303
60.44	72	0.252	0.132	125.7	0.261	0.182	171	3165	33
62.18	74	0.252	0.128	126.5	0.258	0.149	155	2306	22
63.99	77	0.252	0.124	127.3	0.255	0.116	1905	1278	6
65.89	78	0.252	0.119	128.2	0.247	0.084	14	305	1

Table 3.3: Neutron fluence values and their associated uncertainties for each energy bin for ^{7}Li, ^{9}Be and ^{12}C targets obtained from the analysis of the measured data.

E_n (MeV)	$\phi_{^7Li}$ n/MeV.cm^2	u($\phi_{^7Li}$) n/MeV.cm^2	$\phi_{^9Be}$ n/MeV.cm^2	u($\phi_{^9Be}$) n/MeV.cm^2	$\phi_{^{12}C}$ n/MeV.cm^2	u($\phi_{^{12}C}$) n/MeV.cm^2
5.36	398	12	3920	87	6856	149
5.63	903	31	6447	198	14052	426
5.92	1256	57	9738	412	20485	863
6.23	1445	79	11608	607	25992	1355
6.56	2641	174	20777	1340	48308	3110
6.93	3298	256	25013	1911	59074	4507
7.32	2270	208	16453	1479	40038	3593
7.75	1685	185	12841	1381	30693	3294
8.22	2841	344	20147	2415	48341	5789
8.65	3537	481	24306	3278	59574	8027
9.2	3143	333	21608	2263	52367	5478
9.6	3309	410	32755	4022	55540	6817
10.03	3678	470	24486	3103	59398	7522
10.49	3335	493	22385	3285	56496	8286
10.97	2997	463	19928	3057	50241	7701
11.5	2999	516	19134	3272	48901	8356
12.06	2581	498	16293	3126	42508	8151
12.67	2475	485	15478	3017	43019	8380
13.32	2198	442	14252	2844	34588	6897
14.02	1944	427	12347	2695	33101	7218
14.78	1811	401	11284	2482	30083	6610
15.61	1705	385	10160	2278	27601	6182
16.51	1756	402	10287	2335	28163	6385
17.49	1557	380	9321	2257	25681	6211
18.56	1533	353	2645	606	24755	5635
19.73	1699	376	2974	656	27302	5990
21.02	1895	388	2601	531	29887	6058
22.43	2358	455	3525	678	36043	6890
24	2137	392	11787	2141	31853	5780
25.75	2507	428	13240	2241	36208	6123
27.69	2679	428	13906	2206	37072	5876
29.87	2789	409	13405	1951	36834	5355
32.31	2724	367	13176	1758	35049	4670
35.08	3117	371	14838	1750	36750	4329
38.23	3403	349	15332	1559	33809	3434
41.83	3983	356	17886	1585	24546	2174
45.97	3767	272	26837	1910	12319	879
50.78	3697	206	49095	2689	1179	68
56.42	2982	118	61599	2349	976	41
60.44	3244	46	60038	823	626	10
62.18	3599	42	53538	604	511	7
63.99	56461	499	37878	335	178	3
65.89	591	6	12876	102	1	0

Chapter 4

Results and discussion

4.1 Beam profile

This section present results obtained from FLUKA calculations described in chapter 2. In Fig 4.1 neutron fluence obtained from interaction of 200 MeV proton beams of different profiles (halo, pencil and divergency) with a 10 mm thick ^{9}Be target are given. Clearly,the spectra obtained from the interactions of the pencil (Fig.4.1(b)) and diverging (Fig.4.1(c)) beams with the target have the same trend (shape) while the spectra obtained from interactions of the halo beam with the target (Fig.4.1(a)) exhibit a different shape in that it shows prominent peak at high neutron energies at about 150 MeV - 200 MeV, followed by a decrease in the neutron fluence (continuum region) at neutron energies below 150 MeV. Therefore, of the three beam profiles investigated in this study one can deduce that the halo beam is better option for the production of neutrons at high energies compared to the pencil and diverging profiles. Hence, the halo beam was chosen for the purpose of this study.

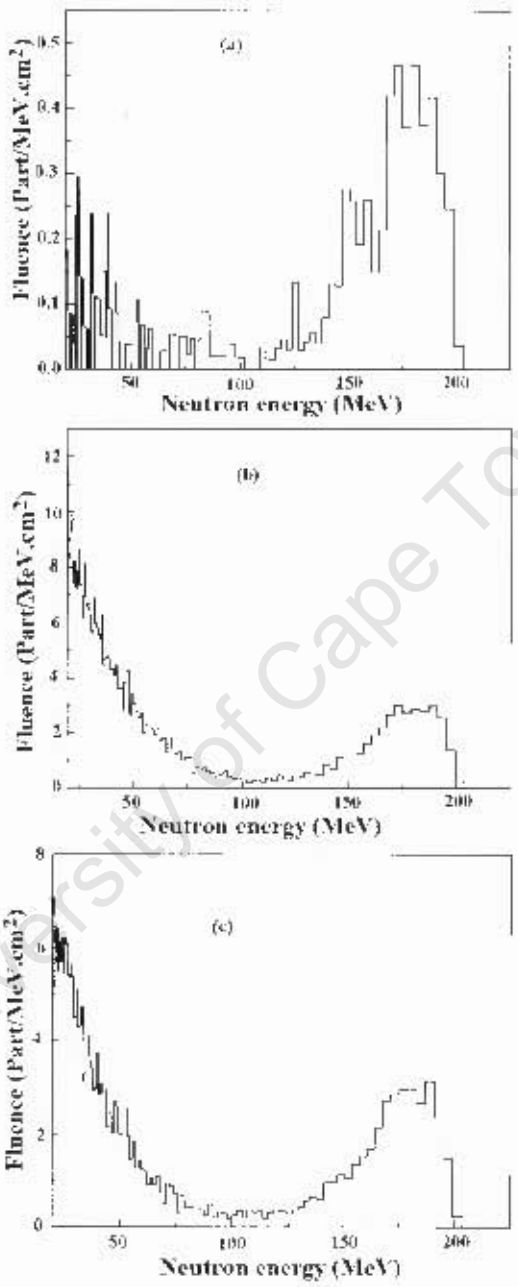

Figure 4.1: FLUKA results of the neutron fluence obtained from the interaction of 200 MeV proton beams of different profile: (a) halo, (b) pencil and (c) diverging beam, with a 10 mm thick beryllium 9 (^9Be) target at zero degree emission angle with respect to the beam axis.

4.2 Neutron emission angle

The results obtained from the production of neutrons in the interaction of 200 MeV protons with a 10 mm thick ^{9}Be target at different emission angles are presented in Fig. 4.2

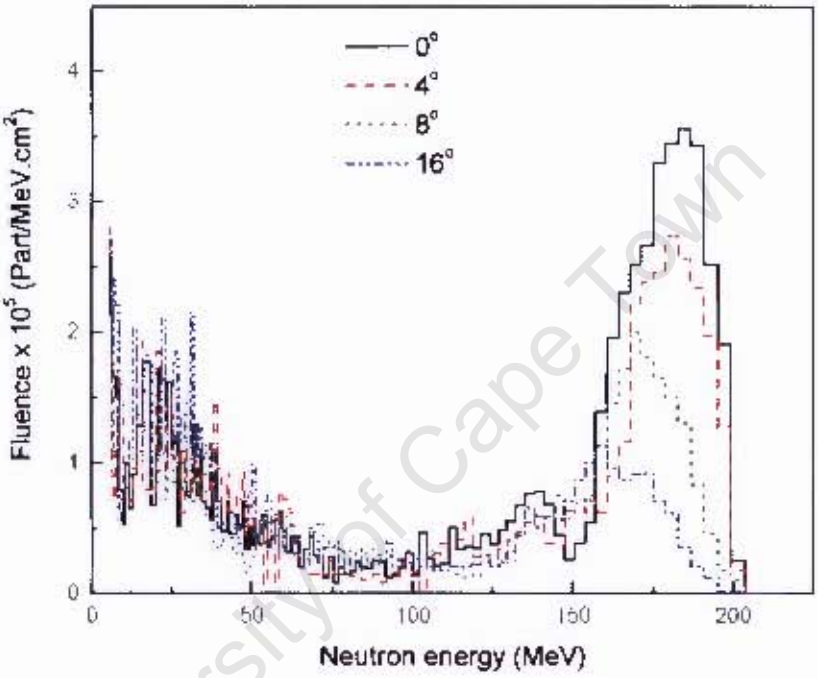

Figure 4.2: Results of FLUKA calculations for the neutron energy spectra obtained from the interaction of 200 MeV proton beams impinging on a 10 mm thick ^{9}Be target at emission angles of 0, 4, 8 and 16 degrees.

As expected, the spectra follow the same shape in that they all exhibit a peak at energies above 150 MeV, followed by a continuum (plateau) at energies 150 MeV - 50 MeV and a slight increase below 50 MeV. Most importantly, the neutron fluence decreases with increasing emission angle, especially around the peak region. In addition, the peak tends to broaden and/or shift towards lower energies with increasing emission angle.

4.3 Production of neutrons from different targets

The neutron fluence spectra were obtained by simulating the interaction of 66 MeV, 100 MeV and 200 MeV proton beam with different targets lithium-7 (^{7}Li), beryllium-9 (^{9}Be) and carbon-12 (^{12}C) of thicknesses 5 mm and 10 mm, respectively.

4.3.1 Results for calculated neutron spectra

Fig. 4.3 shows the results of neutron fluence obtained from 200 MeV, 100 MeV and 66 MeV induced on 10 mm thick (a) ^{12}C, (b) ^{9}Be and 5 mm thick (c) ^{7}Li targets. Overall, the neutron fluence spectra show the expected trend at different proton energies, that is each neutron spectrum has a quasi-monoenergetic peak at an energy lower than the incident proton energy, and also, a small amount of the low-energy continuum is observed.

The effect of the target thickness on the fluence spectra is shown in Fig. 4.4. In this study neutron spectra were obtained from 200 MeV protons on 5 mm and 10 mm thick ^{9}Be, and ^{12}C targets respectively. The spectra obtained from thicker target (10 mm) presented by the solid line in Fig. 4.4(a) and Fig. 4.4 (b) are more broader than the one for the thin target (5 mm) presented by the dotted line. Also one can observe that neutron fluence increases with increasing target thickness, with increase in target thickness protons have more chance to interact with the nuclei, thus, the probability of producing neutrons will be high. However, a slight shift to the low energy region is observed in the spectra obtained form the thick target (10 mm).

Fig. 4.5 shows results for neutron fluence spectra calculated from the interaction of 66 MeV protons with 5 mm ^{7}Li, ^{9}Be and ^{12}C targets. In this case it was observed that the neutrons produced from the three targets cover the entire energy range. The neutron spectrum obtained from the ^{7}Li target has a peak at high energy region while the ^{9}Be target spectrum cover the mid energy region and the one for ^{12}C taget shows a fluence peak shift towards low energy covering wide region. The shift in the neutron spectrum to lower energy for ^{12}C is due to the high energy loss of the protons in the target compared to ^{7}Li and ^{9}Be.

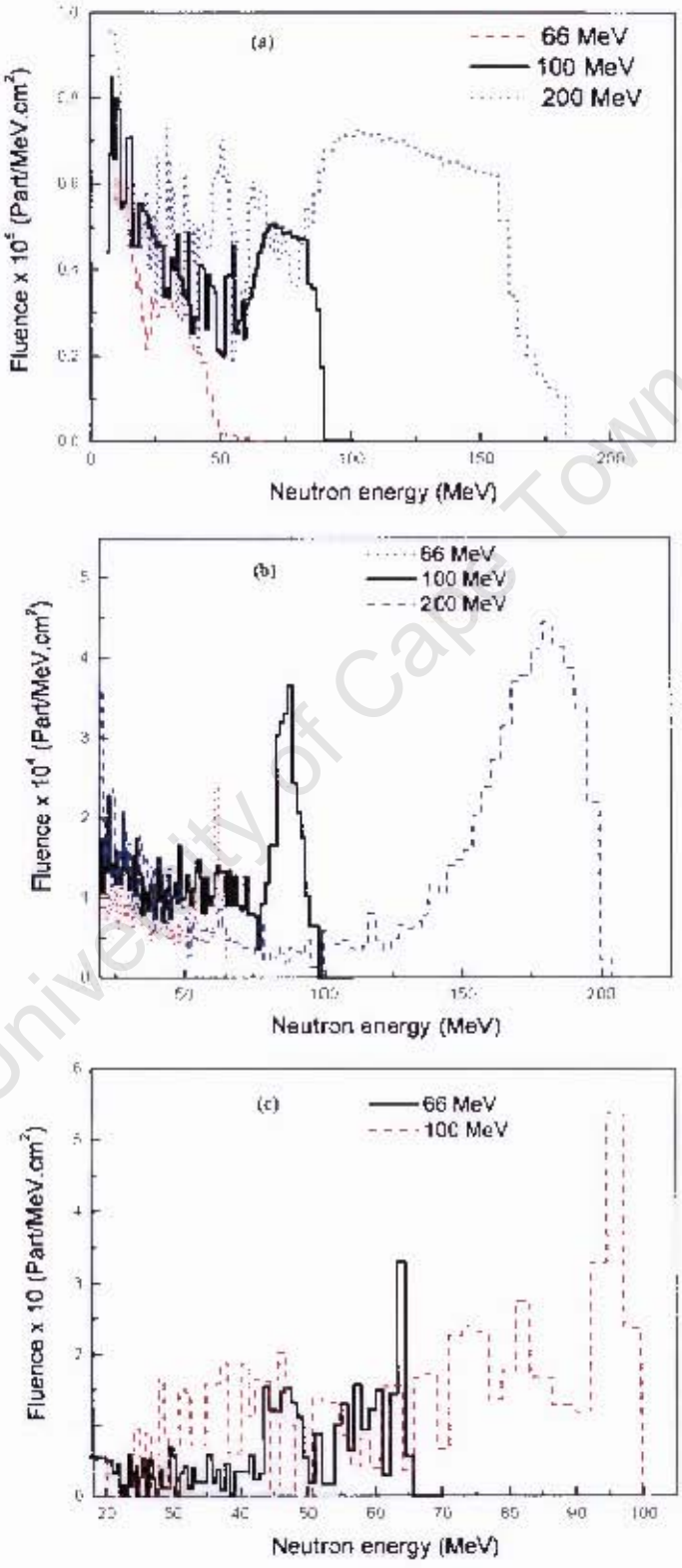

Figure 4.3: FLUKA calculated results for the neutron fluence obtained from 200 MeV, 100 MeV and 66 MeV protons on 10 mm thick (a) ^{12}C, (b) ^{9}Be and 5 mm thick (c) ^{7}Li targets.

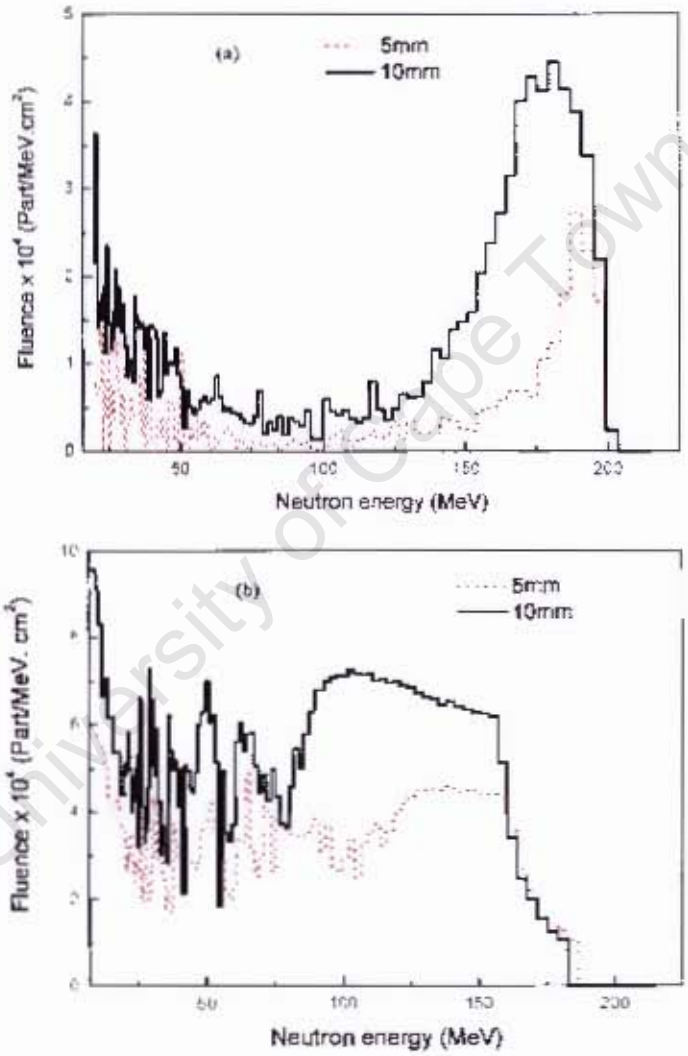

Figure 4.4: Results of FLUKA calculations for the neutron fluence spectra obtained from 200 MeV on 5 mm and 10 mm thick of (a) ^{9}Be and (b) ^{12}C targets.

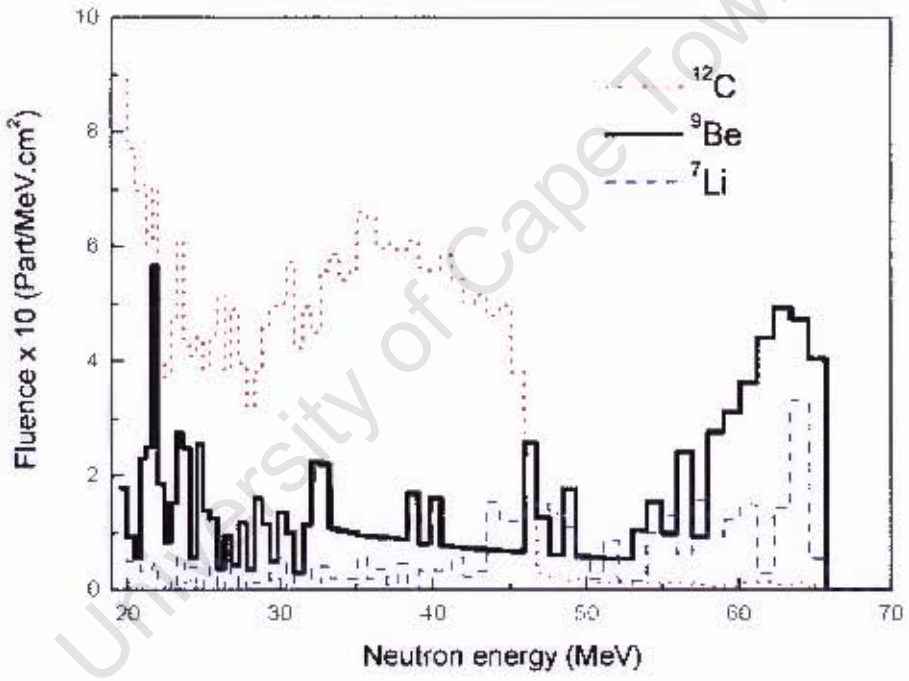

Figure 4.5: Comparision of FLUKA calculations for neutron energy spectra obtained from the interaction of 66 MeV protons impinging on 5 mm thick ^{7}Li, ^{9}Be and ^{12}C targets at emission angles of 0 degree.

4.4 Results from neutron background studies

Results obtained from the simulations of the neutron facility including those obtained from the ^9Be target, havar target ladder, collimator and the rest of the facility (clearing magnet, beam dump, graphite block, etc) are presented in Fig. 4.6 (for more details see section 2.2.5).

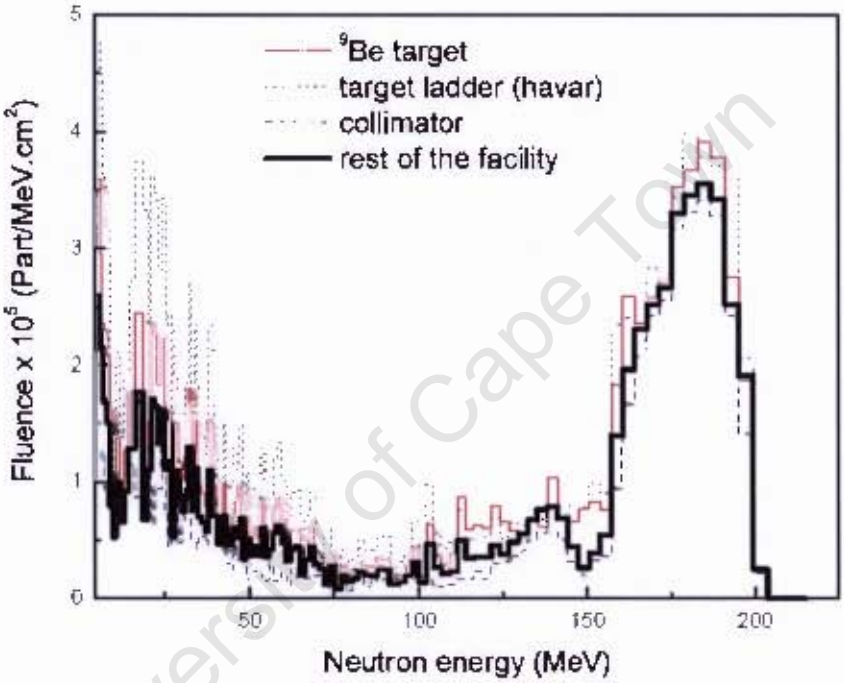

Figure 4.6: Neutron energy spectra obtained from FLUKA calculations of target only, target and the target ladder, collimator and the rest of the facility.

From the figure, the following observations can be deduced:

- All neutron spectra exhibit a peak energies.
- The shape of the spectra changes with the addition of a new material which can be attributed to the fact that the neutrons interact in different way with each material (iron, ^9Be, borated paraflin, etc) depending on the scattering cross section interaction, the larger this cross section, the more interactions will take place with the given material [16].
- The effect of the collimation is clearly observed on the spectrum with a well defined peak at high energy (sharp energy cut on the tail seen on spectrum).

Fig. 4.7 shows the result described in section 2.2.5, for the study of the efficiency of the collimator body as well as at several positions in front of the borated polyethylene door. From the figure

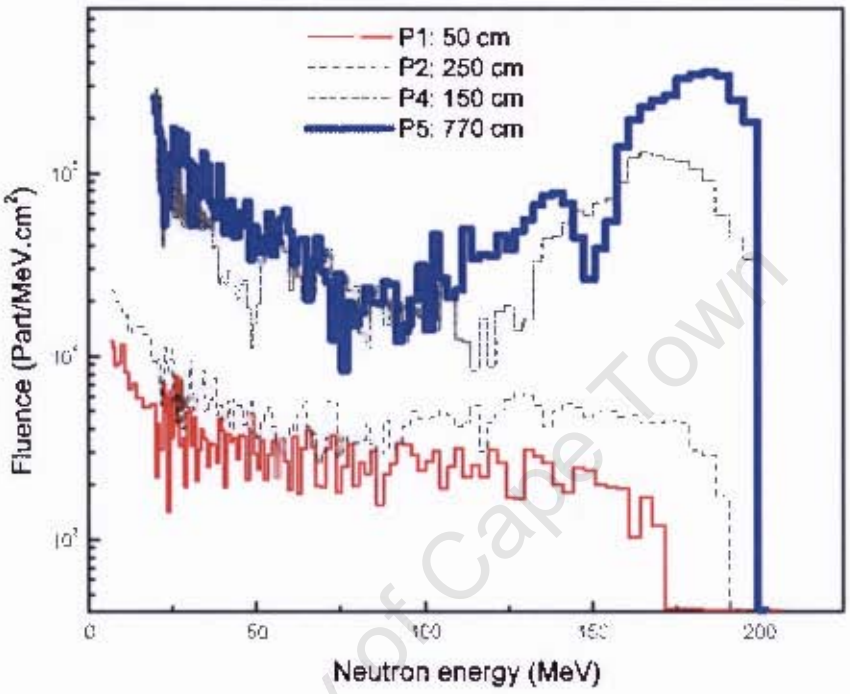

Figure 4.7: Fluence spectra obtained from FLUKA calculations at various positions from the two doors (p1 and p2) leading to the interlock system, in front of the collimator wall (p4) and at 0° and at 770 cm from the target (P5).

one can observed that not all of these neutrons are passing through the door, i.e. some of them might be coming through the opening between the doors and the concrete ceiling. While at the position in front of the collimator wall, (position p3), the amount of the neutrons passing through the collimator body is low. Also, it was observed that the low energy neutron fluence increases at distance further away from the wall (position p4).

Chapter 5

Conclusion

5.1 Comparison of calculated and measured neutron fluence

The neutron fluence spectra were obtained by simulating the interaction of a 66 MeV proton beam with different targets: ^{7}Li, ^{9}Be and ^{12}C of thickness of 1, 10 and 10 mm, respectively. These thickness were used in order to compare with experimental data discussed in Chapter 3. The neutron fluence were calculated at the distance of 7.7 m and emission angle of 0° with respect to the beam axis. The FLUKA results were compared with those obtained experimentally in Fig.5.1(a) - (c). In all cases, the calculated results were normalized to the measured data. From these figures, one can immediately deduce that p+^{7}Li is an ideal reaction for the production of fast quasi-monoenergetic neutron beams, whereas the p+^{12}C and p+^{9}Be reactions are respectively ideal for the production of low energy neutrons, and for the production of neutron beams with a wide energy spread, however overall, the agreement between the calculated and measured data is satisfactory in the sense that the calculated data reproduces the same shape as the measured data.

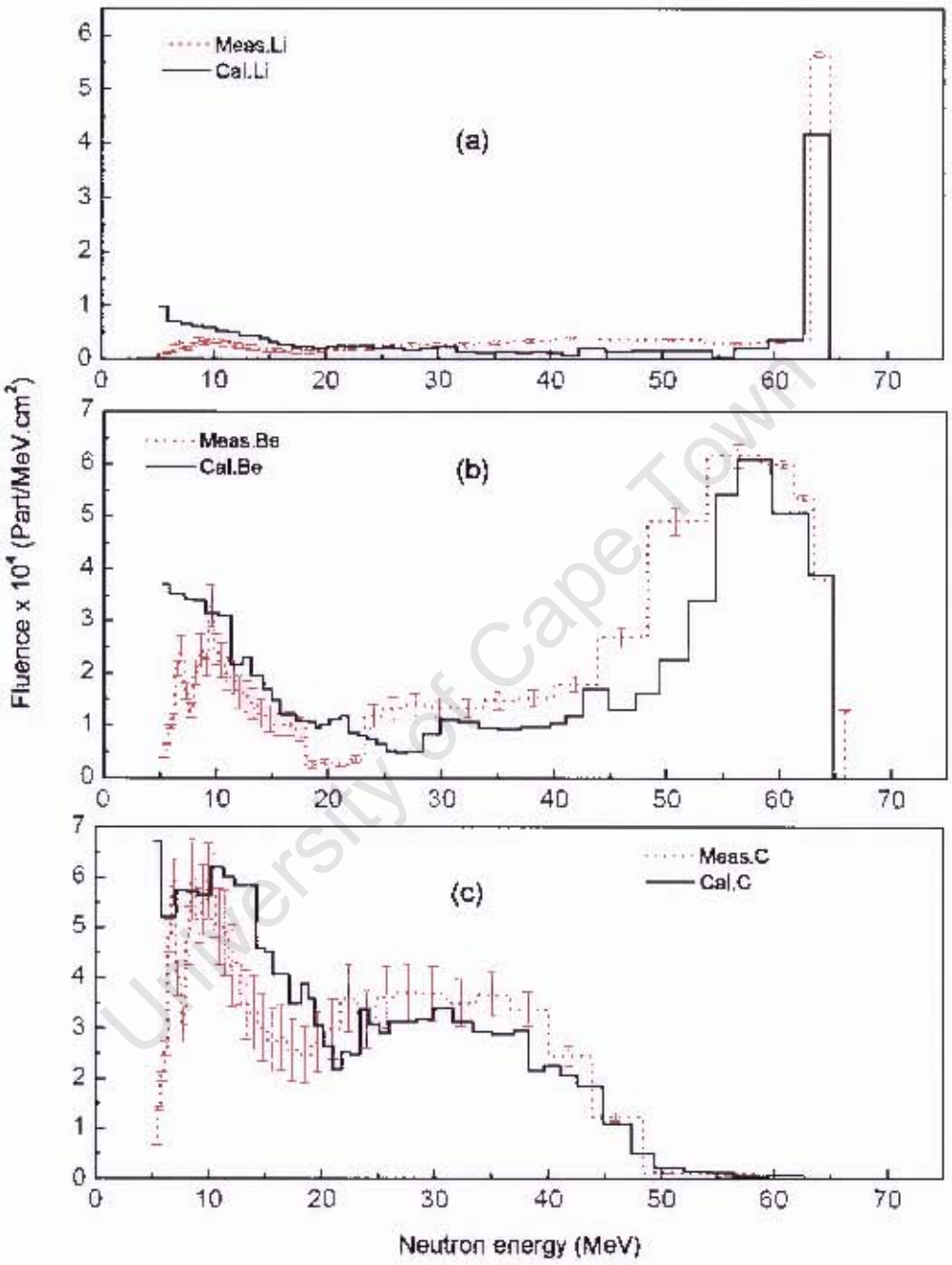

Figure 5.1: Comparison of neutron fluence obtained from FLUKA calculations (solid line) and experimental data (dotted line) [31, 58] for proton interactions with (a) ^{7}Li, (b) ^{9}Be and (c) ^{12}C.

5.2 Proposed modification to the current facility

Further modifications to the facility were made on two different areas, the passage and the height of the two doors. This modifications have been done in order to observe the effect of the secondary neutrons produced on the target area and going through the passage and above the two doors to the experimental area. For this purpose, 8 blocks of borated polyethylene were introduced in different positions as shown in Fig 5.2, and the height of the door was also increased by 50 cm.

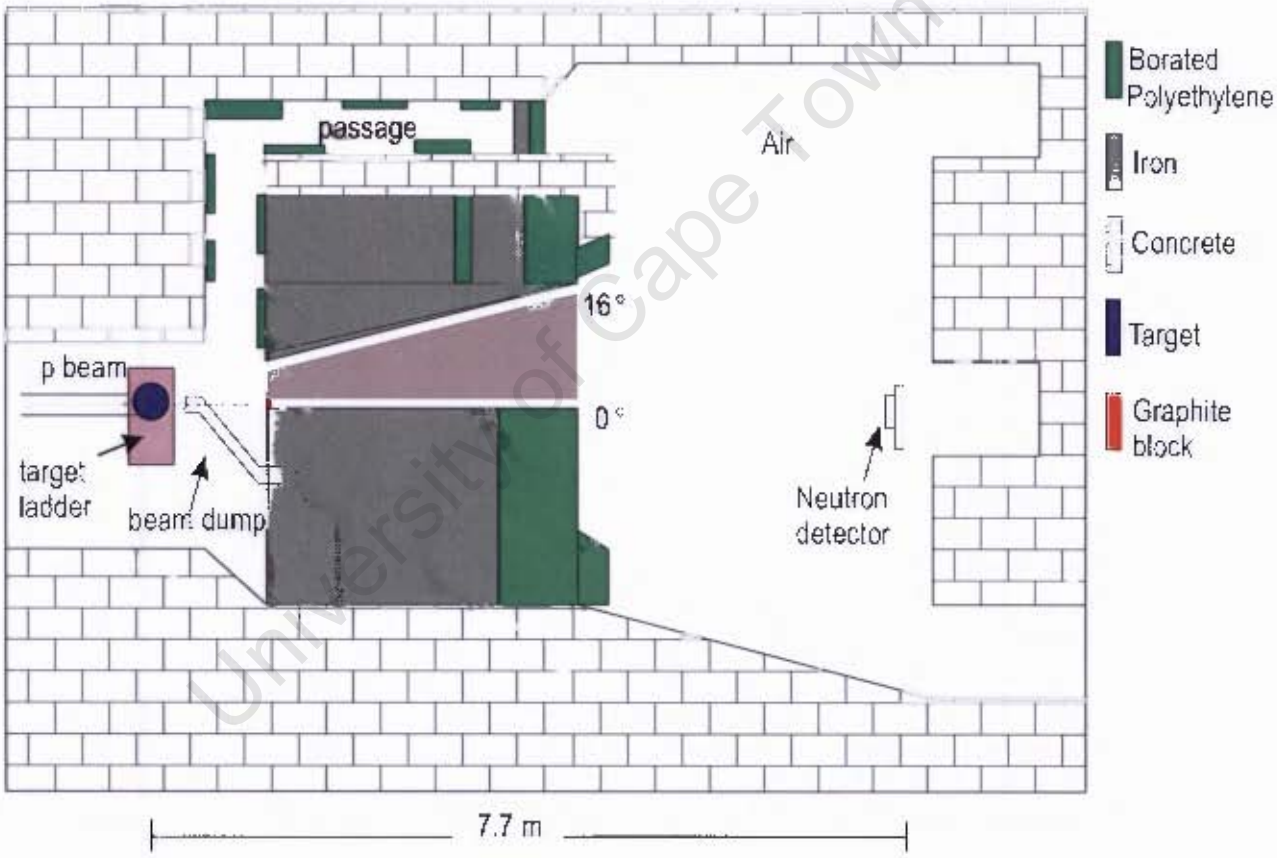

Figure 5.2: Schematic diagram of iThemba LABS neutron facility with the proposed modifications.

Fig 5.3 shows the comparison of the calculated neutron spectra for the current facility (solid line) and the proposed modifications (dotted line). The effect of the above mentioned modification to the current design is most more apparent neutron at energy below 150 MeV, where the neutron fluence is decreased by factor of 1.7 (43 %). From this result one can deduced that the effect of secondary neutrons which are contribute to the measured neutron fluence in the experimental area can be reduced by making a suitbale modification to current desgin of the facility.

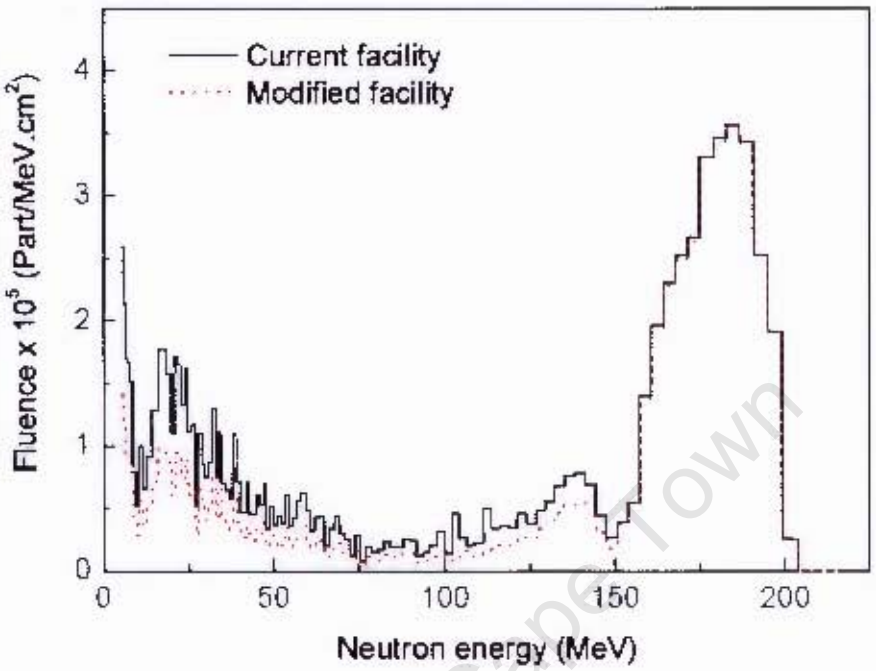

Figure 5.3: Comparison between fluence obtained from the current facility setup (solid line) and the proposed modifications to the current facility (dotted line).

5.3 Summary

This work was based on the neutron facility at iThemba LABS with the focus on the effect of secondary neutrons produced from the interaction of primary particle with the structural parts of the facility on the neutron fluence spectrum. Also, to investigate whether the present geometry of the neutron facility has a contribution to the production of these secondary neutrons.

FLUKA Monte Carlo radiation transport code simulations and experimental measurement have been done to study the neutron spectra at different neutron energies (200, 100 and 66 MeV). In order to study these effects, the entire facility as it is was studied. The validity of the code was determined by studying the effect of varying the neutron emission angles, incident proton energies, and targets with different thicknesses. Study of the neutron background in the facility was carried out in several stages by calculating the neutron fluence spectrum when introducing each part of the facility (target, collimator, clearing magnet, etc) into the geometry card in the input file. The expected trends for both the validity test and neutron background studies were observed.

Based on the results obtained for the neutron background studies, it was clear that there are secondary neutrons escaping above the two doors which have an effect on the neutron fluence. Further modification to the design of the current facility using FLUKA suggest that the effect of the secondary neutrons could be reduced.

The analysis of the experimental measurement for the neutron fluence was performed. Neutron fluence obtained from the interaction of 66 MeV protons with Li, Be and C targets measured by the time of flight technique using NE213 scintillation detector were compared with those calculated using FLUKA. The simulated results obtained show the correlation with experimental data.

The validation test and the neutron background studies carried out using FLUKA show that it is a reliable tool for simulating neutron facility. This is further aided by the agreement of experimental results with results from calculation using FLUKA.

5.4 Future work

As shown from earlier simulated modifications, more work is required to be done in the neutron facility in order to reduce the effect of secondary neutrons on the neutron fluence spectrum. Ideas from this work will be used to further study different modifications that can be achieved so as to improve on the output of the neutron facility.

Appendix A

FLUKA files

A.1 Input file used to calculate neutron fluence obtained from 66 MeV protons on 1 mm ^{7}Li target in the neutron facility

```
*...+....1....+....2....+....3....+....4....+....5....+....6....+....7....+....8
TITLE
Neutron fluence from a proton-irradiated Li target
*...+....1....+....2....+....3....+....4....+....5....+....6....+....7....+....8
BEAM          -0.066       0.0       0.0       0.1       0.0      -1.0PROTON
BEAMPOS          0.0       0.0       0.0
*
GEOBEGIN                                                              COMBNAME
  0 0                     A simple Li target inside vacuum
RPP body1 -5000000.0 +5000000.0 -5000000.0 +5000000.0 -5000000.0 +5000000.0
RPP body2 -1000000.0 +1000000.0 -1000000.0 +1000000.0    -1000.0 +1000000.0
RPP b3        -673.0     +750.5     -200.0     +200.0     -200.0     +1300.0
RPP b4        -373.0     +550.5     -150.0     +150.0     -200.0      +900.0
RPP b5         -1.25      +1.25      -1.25      +1.25     +773.2      +774.0
```

RPP b6	-192.5	+302.5	-149.0	+149.0	203.2	+503.2
RPP b7	-45.5	+162.5	-149.0	+149.0	+203.2	+503.2
RCC b8	0.0	0.0	203.2	0.0	0.0	300.0
	2.5					
RCC b9	0.0	0.0	203.2	0.0	0.0	5.0
	2.5					
RPP b10	-45.5	-2.5	-149.0	+149.0	+488.2	+503.2
RPP b11	+2.5	+162.5	-149.0	+149.0	+500.5	+503.2
RPP b12	+2.5	+162.5	-149.0	+149.0	+485.5	+500.5
RPP b13	+2.5	+162.5	-149.0	+149.0	+470.5	+485.5
RPP b14	+2.5	+162.5	-149.0	+149.0	+470.5	+475.5
RCC b15	30.0	0.0	203.2	100.0	0.0	304.5
	2.5					
RCC b16	30.0	0.0	203.2	2.0	0.0	5.0
	2.5					
RCC b17	7.5	0.0	203.2	25.0	0.0	304.5
	2.5					
RCC b18	15.0	0.0	203.2	50.0	0.0	304.5
	2.5					
RCC b19	22.5	0.0	203.2	75.0	0.0	304.5
	2.5					
RPP b20	+193.5	+302.5	-149.0	+149.0	+503.2	+568.2
RPP b21	-192.5	-45.5	-149.0	+149.0	+503.2	+568.2
RPP b22	-65.0	+65.0	-150.0	+150.0	+900.0	+1200.0
RPP b23	+390.5	+550.5	-150.0	+150.0	+900.0	+1200.0
RPP b24	-373.0	-225.0	-150.0	+150.0	+900.0	+1300.0
RPP b25	+380.0	+550.0	-150.0	+150.0	-200.0	+503.2
RPP b26	-373.0	-192.5	-150.0	+150.0	-200.0	+600.0
RPP b27	+302.5	+380.0	-150.0	+150.0	+497.7	+503.2
RPP b28	+302.5	+380.0	-150.0	+150.0	+492.2	+497.7
RPP b29	+377.5	+380.0	-1.5	+1.5	100.0	+202.0
RPP b30	+50.0	+380.0	-150.0	+150.0	-200.0	+100.0

```
RPP b31       -192.0      -50.0     -150.0     +150.0     -200.0     +100.0
RPP b32        -50.0      +50.0     -150.0     +150.0     -200.0     -100.0
RPP b33         -2.0       +2.0      -9.75      +2.25       0.0        0.5
RPP b34        -0.05      +0.05      -0.05      +0.05       0.0        0.1
END
* black hole
regBH1    5     +body1 -body2
* vacuum around
regVA2    5     +body2 -b3
* outside concrete wall
regCo3    5     +b3 -b4 -b16 -b17 -b18 -b19 -b20 -b21 -b22 -b23
* room filled by air
regAi4    5     +b4 -b5 -b6 -b24 -b25 -b26 -b27 -b28 -b29 -b30 -b31 -b33
* detector
regAi5    5     +b5
* concrete
regCo6    5     +b6 -b7 -b8
* Fe
regFe7    5     +b7 -b8 -b10 -b11 -b12 -b13 -b14 -b15 -b16 -b17 -b18 -b19
* Air inside the collimator
regAi8    5     +b8 -b9
* graphite inside colllimator 0deg
regGr9    5     +b9
* borated paraffin
regPa10   5     +b10
* boron carbide
regBc11   5     +b11 -b15 -b16 -b17 -b18 -b19
* borated paraffin
regPa12   5     +b12 -b15 -b16 -b17 -b18 -b19
* Air
regAi13   5     +b13 -b14 -b15 -b16 -b17 -b18 -b19
* boron carbide
```

```
regBc14   5     +b14 -b15 -b16 -b17
* Air inside the collimator 16 deg
regAi15   5     +b15 -b16
* graphite inside collimator
regGr16   5     +b16
* collimat0r for 4deg
regAi17   5     +b17
* collimat0r for 8deg
regAi18   5     +b18
* collimat0r for 8deg
regAi19   5     +b19
* concrte front experimental area 1
regCo20   5     +b20
* concrete front experimental area 2
regCo21   5     +b21
* detecting area (B)
regAi22   5     +b22
* storge area (C)
regAi23   5     +b23
* door to outside the facility (A)
regAi24   5     +b24
* concrete near to the inside door 1
regCo25   5     +b25
* concrete near to outside door 2
regCo26   5     +b26
* borated paraffin door
regPa27   5     +b27
* Fe door
regFe28   5     +b28
* B4C front hot area
regBc29   5     +b29
* concrete hot area
```

```
regCo30   5     +b30
* air-hot area
regCo31   5     +b31
* concrete hot area
regCo32   5     +b32
* target ladder (Al)
regAl33   5     +b33 -b34
* Li target
regLi34   5     +b34
END
GEOEND
*...+....1....+....2....+....3....+....4....+....5....+....6....+....7....+....8
MATERIAL                          0.001225      24.0                    AIR
COMPOUND  -0.0009256       7.0-0.0002837       8.0-0.0000157       18.AIR
MATERIAL        24.0    51.996      7.19      26.0                    CHROMIUM
MATERIAL                             7.85      27.0                    STEEL
COMPOUND       -0.98      11.0     -0.01      26.0   -0.0012       25.STEEL
COMPOUND     -0.0008       6.0                                        STEEL
MATERIAL        19.0   39.0983     0.862      28.0                    POTASSIU
MATERIAL         0.0       0.0      2.35      29.0        0.0        0.CONCRETE
COMPOUND       -0.01       3.0    -0.001       6.0 -0.529107        8.CONCRETE
COMPOUND      -0.016      19.0    -0.002       9.0 -0.033872       10.CONCRETE
COMPOUND   -0.337021      14.0    -0.013      28.0    -0.044       21.CONCRETE
COMPOUND      -0.014      11.0                                        CONCRETE
MATERIAL         5.0    10.811      2.34      30.0                    BORON
MATERIAL                             0.930     31.0                    PARAFFIN
MATERIAL                             2.52      32.0                    BORCARBD
MATERIAL                           0.9449      33.0                    PARFINBC
COMPOUND   -0.148605       6.0 -0.851395       3.0                    PARAFFIN
COMPOUND     -0.7826      30.0   -0.2173       6.0                    BORCARBD
COMPOUND      -0.975      31.0    -0.025      32.0                    PARFINBC
MATERIAL         3.0     6.941     0.534      34.0                    LITHIUM
```

```
MATERIAL         6.0    12.011       1.7       6.0                    CARBON
*...+....1....+....2....+....3....+....4....+....5....+....6....+....7....+....8
*  External Black Hole
ASSIGNMAT   BLCKHOLE  regBH1
*  Vacuum
ASSIGNMAT   VACUUM    regVA2
* outside wall
ASSIGNMAT   CONCRETE  regCo3
* room air inside
ASSIGNMAT   AIR       regAi4
* air
ASSIGNMAT   AIR       regAi5
* Concrete
ASSIGNMAT   CONCRETE  regCo6
* air
ASSIGNMAT   IRON      regFe7
ASSIGNMAT   AIR       regAi8
* graphite
ASSIGNMAT   CARBON    regGr9
ASSIGNMAT   PARFINBC  regPa10
ASSIGNMAT   BORCARBD  regBc11
ASSIGNMAT   PARFINBC  regPa12
ASSIGNMAT   AIR       regAi13
ASSIGNMAT   BORCARBD  regBc14
ASSIGNMAT   AIR       regAi15
ASSIGNMAT   CARBON    regGr16
ASSIGNMAT   AIR       regAi17
ASSIGNMAT   AIR       regAi18
ASSIGNMAT   AIR       regAi19
* conrete wall 1
ASSIGNMAT   CONCRETE  regCo20
* conrete wall 2
```

```
ASSIGNMAT   CONCRETE  regCo21
* detecting area
ASSIGNMAT   AIR       regAi22
* storge
ASSIGNMAT   AIR       regAi23
* to outside door
ASSIGNMAT   AIR       regAi24
* concrete 1
ASSIGNMAT   CONCRETE  regCo25
* concrete 2
ASSIGNMAT   CONCRETE  regCo26
* borated pararffin door
ASSIGNMAT   PARFINBC  regPa27
* iron door
ASSIGNMAT   IRON      regFe28
* B4C hot area
ASSIGNMAT   BORCARBD  regBc29
* concrete around hot area
ASSIGNMAT   CONCRETE  regCo30
* air hot area
ASSIGNMAT   CONCRETE  regCo31
* concrete around hot area
ASSIGNMAT   CONCRETE  regCo32
* target ladder(Al)
ASSIGNMAT   ALUMINUM  regAl33
* Li target
ASSIGNMAT   LITHIUM   regLi34
*...+....1....+....2....+....3....+....4....+....5....+....6....+....7....+....8
* e+e- and gamma production threshold set at 10 MeV
EMFCUT        -0.010     0.010       1.0       AIR                     PROD-CUT
* score in each region energy deposition and stars produced by primaries
SCORE         ENERGY  BEAMPART
```

```
* Boundary crossing fluence in the middle of the target (log intervals, one-way)
USRBDX          99.0       8.0     -47.0   regLi34    regAi4      6.25nFluenUD
USRBDX         0.066     0.005      43.0  0.015256       0.0      10.0&
* Boundary crossing current in the middle of the target (log intervals, one-way)
*...+....1....+....2....+....3....+....4....+....5....+....6....+....7....+....8
RANDOMIZE        1.0
*...+....1....+....2....+....3....+....4....+....5....+....6....+....7....+....8
START    100000000.0
STOP
```

A.2 Calculated neutron fluence data

Table A.1: Calculated neutron fluence obtained from 66 MeV protons on 1 mm ^{7}Li target.

Number	Neutron energy (MeV)	Neutron fluence Part/MeV.cm^2
1	65.89 0	0.0
2	63.72259	41722.57931
3	61.52378	3677.95814
4	57.35116	2039.98204
5	55.3722	377.24133
6	53.46153	1649.53344
7	50.61679	1543.04562
8	48.11607	1553.23077
9	46.45578	1358.36671
10	43.30509	2023.67143
11	41.8108	812.78314
12	40.36808	1331.76568
13	38.97514	1433.14034
14	37.63027	1215.42726
15	36.3318	1357.36241
16	33.86773	1303.64685
17	32.69909	1353.94428
18	30.4814	2408.90255
19	29.42961	2144.88799
20	27.43365	1562.44492
21	26.48703	2033.7595
22	25.57307	2349.20419
23	24.69065	2177.51978
24	23.83867	2482.73468
25	22.2219	2352.97614
26	21.45511	2557.35758
27	20.71478	2440.98254
28	19.6	2236.6011
29	19.1554	2116.67174
30	18.6825	2284.07665
31	17.7713	2368.68538
32	16.4872	2656.6729
33	15.0801	3288.61109
34	14.9183	3796.969
35	13.4986	4407.50163
36	12.8402	4381.42069
37	11.9125	5114.29393
38	10.7788	5229.23957
39	9.7531	5840.8928
40	8.39457	6216.40512
41	7.78801	6655.36512
42	6.5377	7209.21042
43	5.22046	9868.06341

Appendix B

Data reduction

This appendix is a detailed description of the data reduction for the neutron fluence measurement presented in Chapter 3 extracted from the thesis of Dr. Herbert [31].

B.1 Beam profile

The neutron beam profile was achieved using a cylindrical anthracene crystal detector (10 mm diameter x 20 mm length). Horizontal and vertical scans were made across the neutron beam, recording the number of events detected in the crystal for a fixed integrated proton charge. Results of the measurements obtained for the scans, as a function of distance from the center position in the beam are shown in Fig. B.1 The intensity profile of the neutron beam was found to be uniform over a circular area of diameter 50 mm. Thus, the dimensions of the detectors used in the experiments were such that the beam fully illuminated the detectors at all the positions along the beam axis at which measurements were taken.

B.2 Time-of-Flight to neutron energy calibration

The time parameter, T_n, was used to produced the Time-of-Flight, TOF, spectrum shown and discussed in the previous section. Similar spectra were obtained for ^{9}Be and ^{12}C targets. Fig B.2

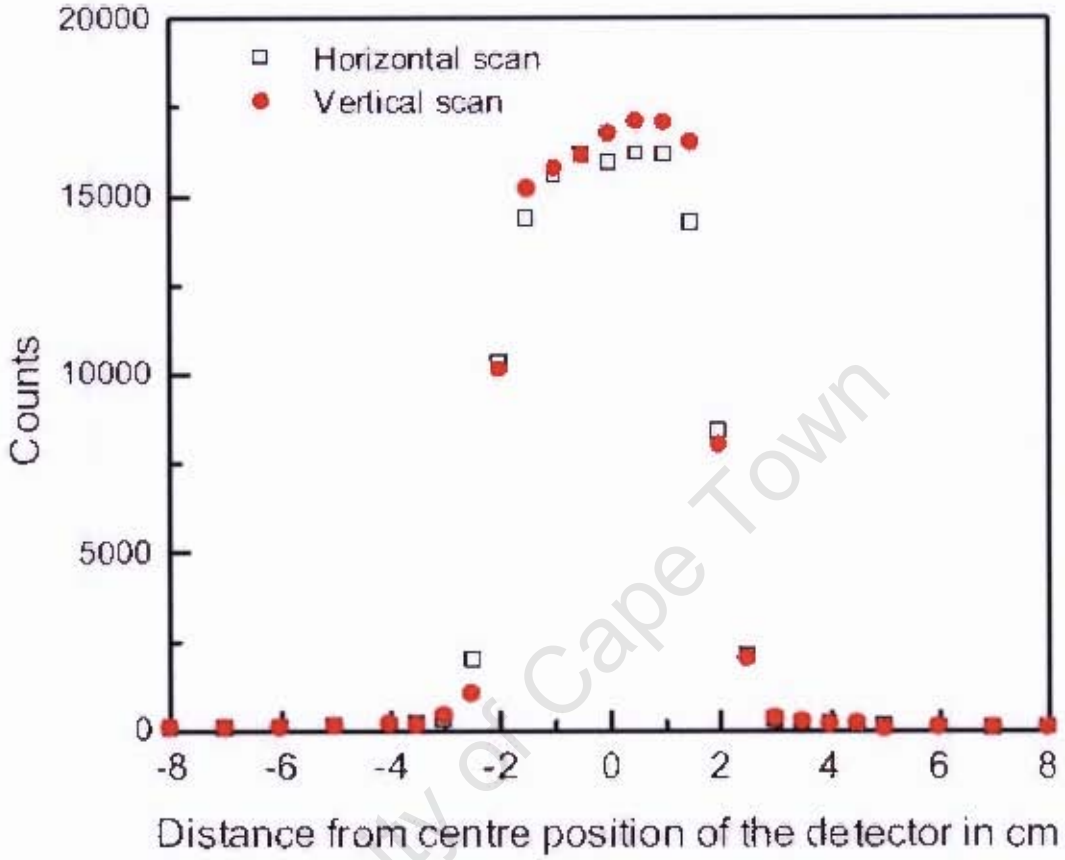

Figure B.1: Beam profile measurements obtained for the horizontal and vertical scans as a function of distance from the center in the 0° neutron beam. The detector was placed in the 0° neutron beam at a distance of 7.7 m from the target [31].

shows the neutron TOF spectra for the three targets. The TOF spectrum of the ^{7}Li target shows that the highest energy neutrons of 64 MeV produced, fall within a sharp high-energy peak. This peak arises principally from the transition to the unresolved ground and first excited states of ^{7}Be in the ^{7}Li(p, n)^{7}Be reaction. The rest of the spectrum consists of a broad lower energy tail, which arises from excitation of the higher states in ^{7}Be or from break up reactions leading to three or more particles in the final state. The TOF spectrum of the ^{9}Be target shows that the highest energy neutrons of 63 MeV target (Q = -1.85 MeV) produced, fall within a broader peak which arises from the transition to the unresolved ground of the first and second excited states of ^{9}Be in the ^{9}Be(p,n)^{9}B reaction.

The TOF spectrum of the ^{12}C target shows that the most energetic neutrons of 48 MeV (Q =

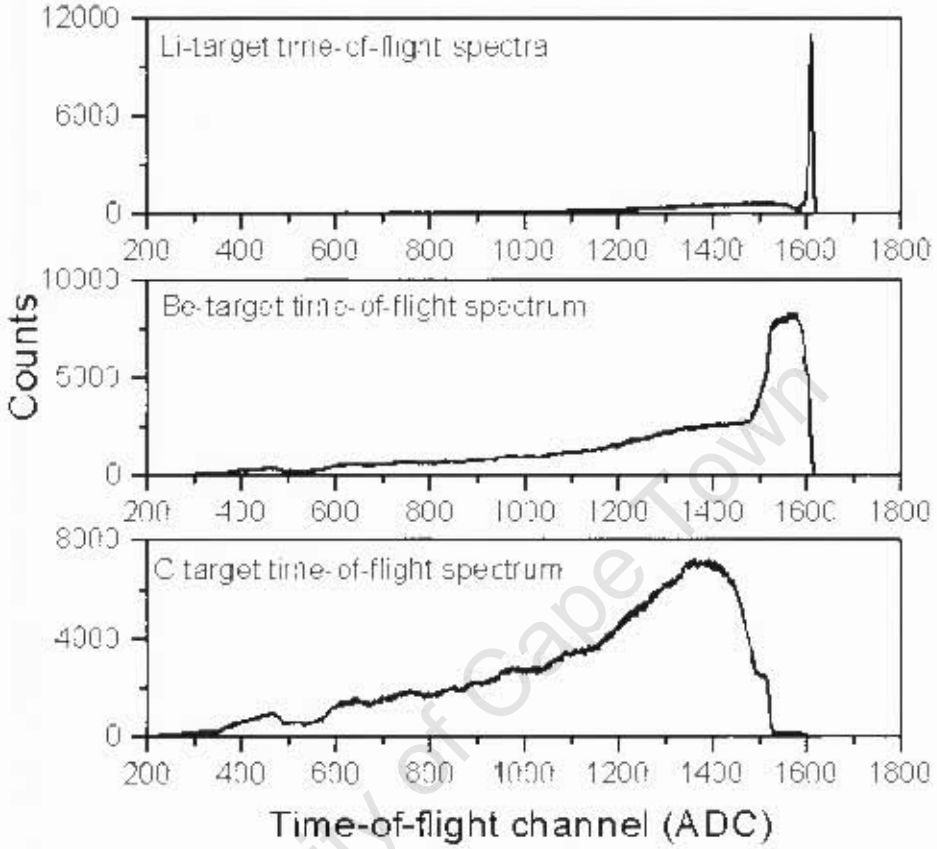

Figure B.2: TOF spectra of Be-target and C-target measured by the NE213 detector for neutrons of energy 5 to 64 MeV. The Li target spectrum is included for reference [31].

-18.12 MeV) arises from the transition to the unresolved ground and excited states of ^{12}B in the ^{12}C(p,n)^{12}B reaction which cannot be resolved by the energy resolution of the detectors. Also, one can observe that the peak in the TOF spectrum of the ^{12}C target is much broader than the peaks in the spectra of ^{7}Li and ^{9}Be. This is because the thicknesses of the ^{12}C and the ^{9}Be is greater than that of the Li. Since ^{12}C target and ^{9}Be have the same thickness, ^{12}C peak is broader than the one for ^{9}Be due to the fact that the atomic number of the ^{12}C is greater than that of ^{9}Be. The humps observed in the TOF spectra between $T = 300$ and 900 ADC channels are attributed to resonances of ^{12}C associated with the 6.5 cm thick graphite block placed in front of the collimator side facing the target.

In order to convert the neutron TOF data from T scale in ADC channels to a time scale in nanoseconds, the time calibration constant (TAC channels per nanosecond) was found as follows: TAC was operated with two known delay cables respectively, and the change in the position of

the neutron peak in the TOF spectrum was recorded, from which a calibration constant of 8.33 channels/ns was calculated. The average energy of the neutrons in the sharp high-energy peak was estimated as follows: For the 66 MeV incident protons on the 1 mm ^{7}Li target, an energy loss of 0.44 MeV was calculated using ELOSS [59], and by assuming linear energy loss through the target. The energy of the proton emerging from the target was therefore calculated to be 65.56 MeV. The energy of the proton at the center of the target was assumed to be halfway between 66 MeV and 65.56 MeV, and was estimated to be 65.78 MeV. Using the Q-value for ^{7}Li(p,n)^{7}B reaction of -1.644 MeV and the reaction kinematic equations [64], the energy of the neutrons at the center of the neutron peak was estimated to be about 64 MeV. The TOF of 64 MeV neutrons over a flight path of 7.7 m was calculated to be 73.14 ns, using the relativistic relationship

$$t = \frac{d}{c\sqrt{1 - \left[\frac{m_0c^2}{E_n - m_0c^2}\right]^2}}. \tag{B.1}$$

The relationship between the neutron TOF scale T in ADC channels and the neutron TOF scale t in nanosecond, is given by

$$E_n = m_0c^2\left(\frac{1}{\sqrt{1 - \left(\frac{d}{\left(\frac{T_{max}}{k_{cal}} - \frac{d}{c} + t_{max}\right)c}\right)^2}} - 1\right). \tag{B.2}$$

where

T: the TOF channel number in ADC;

T_{max}: the position of the most energetic neutrons in ADC;

t_{max}: Neutron flight time of the most energetic neutrons in ns (73.14 ns);

k_{cal}: the time calibration constant in channels/second (8.33 channels/ns);

d: the flight path of the neutrons in meters (7.7 m);

m_o: rest mass of the neutron (939.57 MeV/c^2);

c: the speed of light (3x10^8 m.s^{-1}).

Because the neutron energy will be determined using the TOF method, the overall energy resolution of the neutrons is determined by the timing resolution. Thus, the time resolution of the

detectors is important. By increasing the flight path, improved time (energy) resolution will be obtained. The time resolution, $\Delta t_{\gamma\gamma}$ of the time of flight measurements was determined from the FWHM of the gamma peak in the TOF spectra, produced by proton-induced reactions in the targets. The time resolution at FWHM of the gamma peak was measured as 0.84 ns. The energy resolution, ΔE_n, of the TOF measurements depends on the time resolution and the uncertainty in the flight path, Δd, of the neutrons. In the limit $\frac{\Delta t_\gamma}{T} \frac{\Delta d}{d}$, the energy resolution, ΔE_n is given by

$$\Delta E_n = \left[\left(1 + \frac{E_n}{m_o c^2}\right)\left(2 + \frac{E_n}{m_o c^2}\right) E_n\right] \frac{\Delta t_\gamma}{t} [31], \tag{B.3}$$

This implies energy resolutions of 0.06 MeV at 5.36 MeV, and 1.62 MeV at 64 MeV. Fig. B.3 shows the energy resolution, ΔE_n, as a function of neutron energy, E_n, for neutron energies between 5 to 64 MeV.

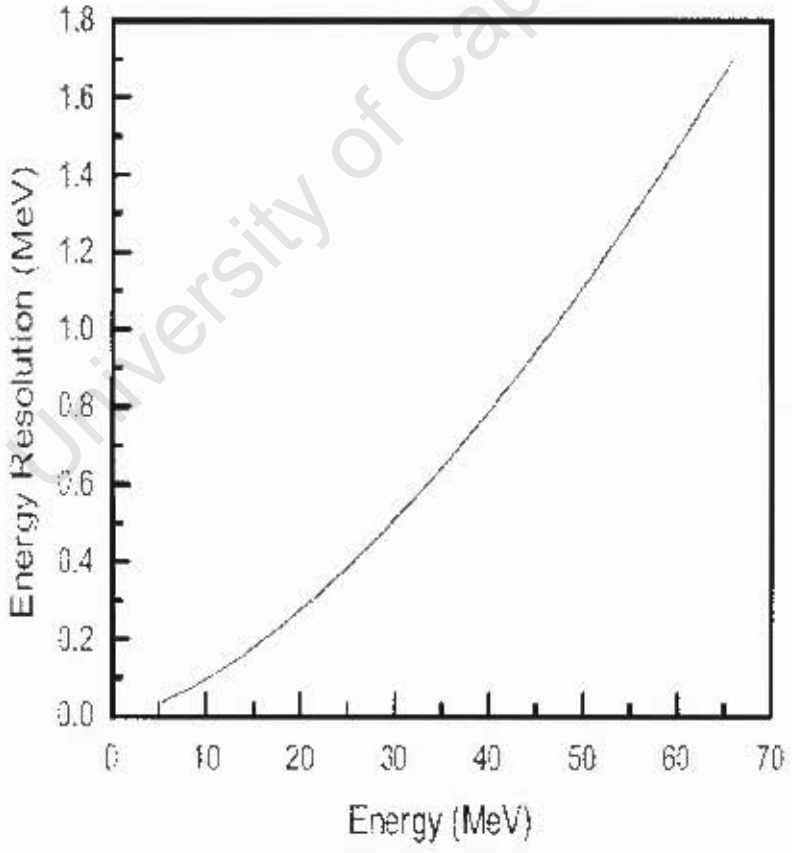

Figure B.3: Energy resolution as a function of the neutron energy between 5 MeV and 64 MeV [31].

B.3 Particle Discrimination

The pulse shape discrimination (PSD) technique was used to identify the different charged particles produced from neutron interactions in NE213 detector medium. This was carried out by computing a scintillation pulse shape parameter, S, from the pulse height, L, and fast component, F, using the equation

$$S = L - kF + C. \tag{B.4}$$

where k and C are arbitrary constants chosen to optimize the differences between the particle loci in a display of L versus S. Fig. B.4 shows a perspective plot of counts (vertical) versus L and S for events detected by the NE213, when exposed to neutrons obtained from 66 MeV protons incident on the 1 mm thick Li-target.

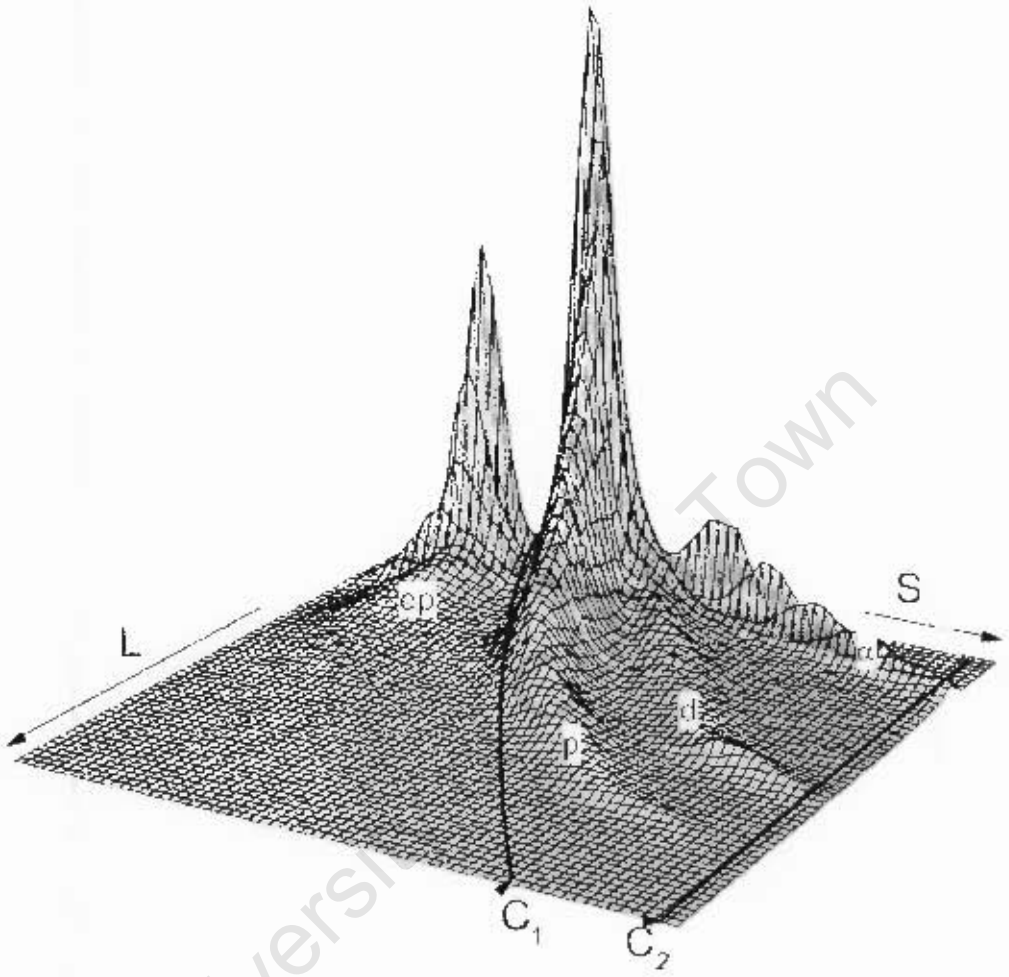

Figure B.4: Perspective views of counts (vertical) as a function of pulse height, L, and pulse shape, S, for the charged particle events detected by NE213 detector when exposed to neutrons from 66 MeV protons incident on the 1 mm thick Li target [31].

It can be seen from this plot that the events corresponding to different ionizing particles lie on well-defined ridges that are resolved in the LS-plane. The ridges shown in Fig. B.4 for the events in NE213 are associated with protons (p) arising from n-p elastic scattering and n-C reactions, deuterons (d), and alphas (α) from n-C reactions [2]. The less prominent ridge (ep) to the left of the (p) ridge arises from the detection of escaping charged particles, mainly protons that exit the scintillator volume.

The figure also shows the LS-cuts, C_1 and C_2, used to separate and select all the proton and heavier charged particle events in the NE213 detector. The events selected by the cuts are

projected into the L axis to produce the pulse height spectrum. Similar projections of these events onto the L-axis were made for ^{9}Be and ^{12}C targets and the corresponding pulse height spectra are shown in Fig. B.5.

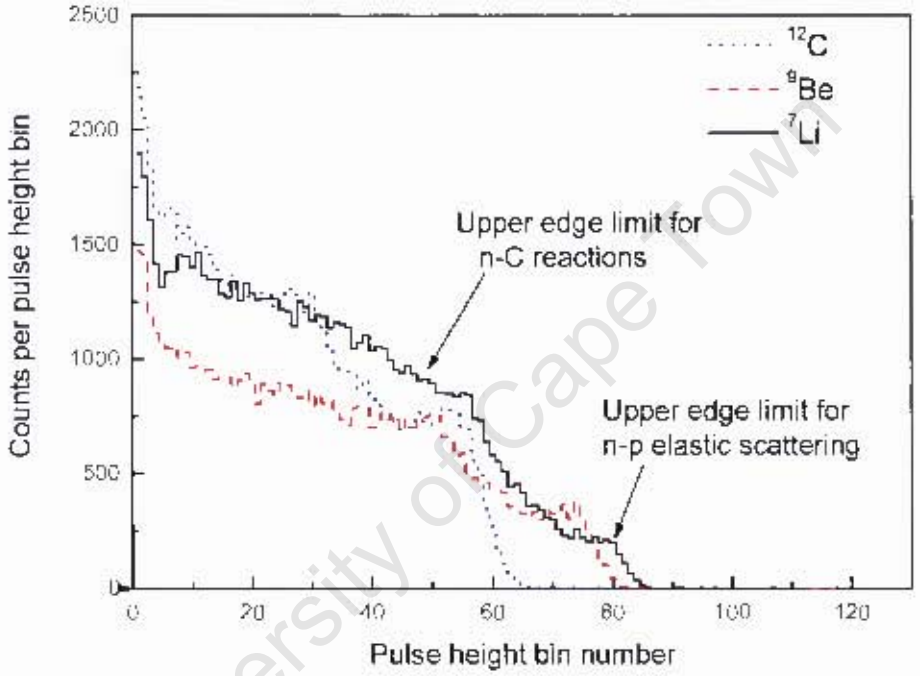

Figure B.5: Pulse height spectrum measured by the NE213 detector for proton and heavier charged particles when exposed to neutrons of energy 5 to 64 MeV produced by 66 MeV protons on the 1 mm thick ^{7}Li target, 10 mm thick ^{9}Be target and 10 mm thick ^{12}C target.

Pulse height spectra in ADC channels (L) and the corresponding time-of-flight spectra in ADC channels (T) were obtained for each target for neutrons of energy 5 to 64 MeV. In the plot the pulse height spectrum of the ^{12}C target has fewer high pulse height events than the spectra of the other targets. This may be attributed to the high Q-value of the ^{12}C(p,n)^{12}N reaction. The spectra has well defined upper edges and one can identify the upper pulse height limits for n-C reactions, and n-p elastic scattering in the respective spectra while the thicker targets have broader upper edges corresponding to a wide range of energies.

B.4 Pulse height spectrum at specific neutron energy

Fig. B.6 shows perspective plot of counts (vertical) versus L (charged particle energy) and T (incident neutron energy) for the events lying within the C_1 and C_2 cuts in Fig. B.4. The main

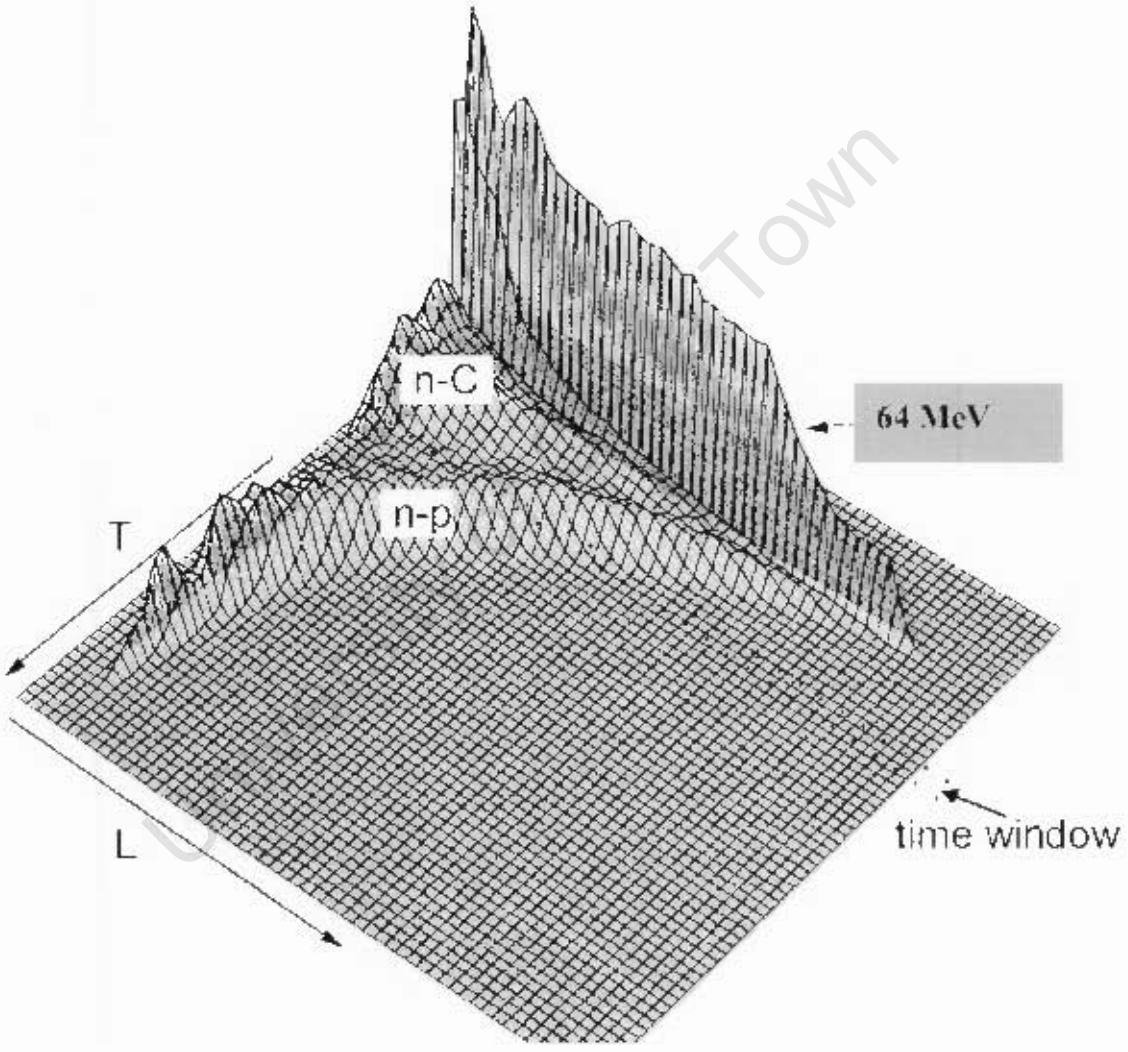

Figure B.6: Perspective views of counts (vertical) as a function of pulse height, L, and Time-of-Flight, T, for the proton and heavier charged particle events detected by NE213 when exposed to neutrons produced by 66 MeV protons incident on the 1 mm thick Li-target. The dashed lines in the plots indicate the time window used to select neutrons of 41 MeV [31].

features for the selected proton and heavier charged particle events shown in LT-plot (fig. B.6) are the curved ridge on the left marking the upper pulse height, L, limit for recoiling protons

from n-p elastic scattering events. The maximum proton energy associated with the n-p ridge edge is equal to the incident neutron energy. The ridges observed on the right side are due to proton events from n-C reactions. The second ridge at lower pulse height is associated with the maximum pulse height for proton recoils from n-C reactions. The strong ridge at the far right corresponds mainly to the intense forward peak of 64 MeV neutrons from the ^{7}Li(p,n)^{7}B reaction. It can be seen in the plot that at low L values, i.e. low neutron energy, the ridges from n-p and n-C are more distinguishable than at high L values; this is due to an increase in escape of protons from the detector with increasing neutron energy. Fig. B.6 also shows an example of a time window setting on the T-axis used to select neutrons of energy E = 41 MeV. The projection of the events in the time window on the I,L-plane onto the L-axis gives the detector response function to neutrons of energy 41 MeV. The corresponding pulse height spectrum obtained at the specific neutron energy (41 MeV) is shown in Fig. B.7. The edge which can be seen is defining

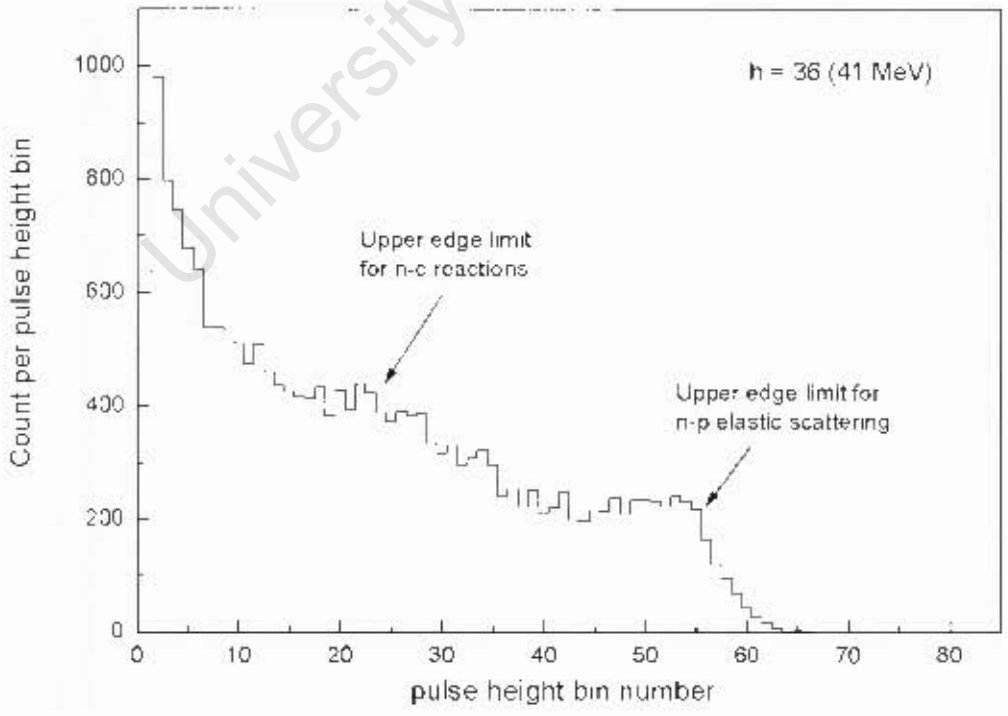

Figure B.7: Pulse height spectrum measured by the NE213 scintillator, when exposed to 41 MeV neutrons. The upper edge of the spectrum is a well-defined function of the neutron energy.

the upper pulse height limit for n-C reactions, n-p elastic scattering is clearly identifiable in the figure, and is a well defined function of neutron energy.

B.5 Neutron detection efficiency of the NE213 detector

The efficiency of neutron detection is an intrinsic property of the detector used and it is a quantity relating the fraction of pulses recorded by the detector with the energy, E_n, to the number of the neutrons incident on the detector (the probability of the detector being able to detect a neutron with energy, E_n)

$$\epsilon(E_n) = \frac{\text{number of detected neutrons}}{\text{number of incident neutrons}}. \tag{B.5}$$

The detection efficiency can be determined either by measurement or by calculation. Many methods have been used for the measurement of detection efficiency [65]. To obtain an unknown neutron energy spectrum the response function for the detector should be measured and then unfolded using the response matrix. Many unfolding codes have been developed over the years, based on several different techniques, such as least-squares adjustments, genetic algorithms or maximum entropy methods [36, 66, 67]. The neutron detection efficiency of the detector for detecting a neutron of a particular energy is the probability of an incident neutron of that energy to produce an acceptable pulse in the detector. Measurement of the neutron detection efficiency in NE213 scintillator requires information about the different probabilities of the interaction of the neutron with the scintillation material. Since the NE213 contains hydrogen and carbon nuclei, a precise knowledge of the n-p and n-C scattering cross sections is important, i.e. for a neutron to be detected it must transfer enough energy to a charged particle for the scintillation pulse to exceed the electronic detection threshold of the detection system.

The detection efficiency $\epsilon_{np}(E_n, L_{np})$, of the NE213 scintillator was determined as a function of neutron energy, E_n, above a pulse height threshold, L_{np}. Table B.1 shows the different factors used to determine the neutron detection efficiency for NE213.

The total number of protons, n_H, per cm^2 presented to the beam by the scintillator is given by the equation 3.4 and was calculated by substituting the values presented on page 35 in equation 3.4, and was found to be 0.252 barn^{-1}. The neutron detection efficiency, ϵ_H, for the NE213

Table B.1: Factors used to calculate the efficiency of NE213 scintillator.

E_n (MeV)	σ_H (barn)	n_H (barn^{-1})	ϕ_{npf}	ϵ_H (10^{-3})	$u(\epsilon_H)$ (10^{-3})
5.36	1.551	0.252	0.081	31.65	2.36
5.63	1.49	0.252	0.122	45.8	2.39
5.92	1.434	0.252	0.173	62.51	2.52
6.23	1.381	0.252	0.213	74.12	2.62
6.56	1.332	0.252	0.254	85.25	2.74
6.93	1.271	0.252	0.294	94.16	2.83
7.32	1.23	0.252	0.334	103.52	2.96
7.75	1.165	0.252	0.37	108.62	2.96
8.22	1.107	0.252	0.405	112.98	3
8.65	1.067	0.252	0.435	116.96	3.04
9.2	1.004	0.252	0.475	120.17	3.06
9.6	0.97	0.252	0.502	122.7	3.09
10.03	0.938	0.252	0.514	121.49	3.02
10.49	0.899	0.252	0.54	122.33	3.01
10.97	0.862	0.252	0.56	121.64	2.98
11.5	0.828	0.252	0.579	120.81	2.92
12.06	0.796	0.252	0.599	120.15	2.89
12.67	0.76	0.252	0.614	117.59	2.8
13.32	0.723	0.252	0.634	115.51	2.74
14.02	0.689	0.252	0.658	114.24	2.68
14.78	0.655	0.252	0.672	110.92	2.58
15.61	0.62	0.252	0.692	108.11	2.49
16.51	0.587	0.252	0.707	104.58	2.38
17.49	0.553	0.252	0.731	101.86	2.3
18.56	0.523	0.252	0.692	91.2	2.05
19.73	0.489	0.252	0.653	80.46	1.8
21.02	0.458	0.252	0.614	70.86	1.58
22.43	0.426	0.252	0.574	61.62	1.36
24	0.397	0.252	0.54	54.02	1.19
25.75	0.368	0.252	0.504	46.73	1.02
27.69	0.337	0.252	0.47	39.91	0.86
29.87	0.307	0.252	0.437	33.8	0.71
32.31	0.281	0.252	0.409	28.96	0.59
35.08	0.255	0.252	0.382	24.54	0.49
38.23	0.23	0.252	0.355	20.57	0.39
41.83	0.206	0.252	0.329	17.07	0.3
45.97	0.184	0.252	0.309	14.32	0.22
50.78	0.163	0.252	0.286	11.74	0.15
56.42	0.144	0.252	0.274	9.94	0.09
60.44	0.132	0.252	0.261	8.68	0.06
62.18	0.128	0.252	0.258	8.32	0.05
63.99	0.124	0.252	0.255	7.96	0.04
65.89	0.119	0.252	0.247	7.4	0.03

scintillator of a particular energy via n-p elastic scattering is [25]

$$\epsilon_H = \phi_{npf}(E_n, L_{np}) \frac{n_H(E_n)\sigma_H}{n_H\sigma_H + n_C\sigma_C} \left[1 - e^{-(n_H\sigma_H + n_C\sigma_C)}\right], \tag{B.6}$$

where

n_H: the number of hydrogen atoms per unit cross sectional area presented to the beam by the scintillator,

n_C: the number of carbon atoms per unit cross sectional area presented to the beam by the scintillator,

$\phi_{npf}(E_n, L_{np})$: the fraction of mono-energetic neutrons of energy E_n detected above pulse height threshold L_{np} that undergo n-p elastic scattering only in the NE213 scintillator,

$\sigma_H(E_n)$: the total cross section for n-p elastic scattering, and

σ_C: the total cross section for all neutron induced reactions with ^{12}C in the scintillator.

As the measurements in the present work were made using cylindrical NE213 of an area of $2\Pi \times 50 \times 50 \times 50$ mm, the thin scintillator approximation was assumed to be valid [60], therefore in this case, the $n_H\sigma_H + n_C\sigma_C$ became $\ll 1$ and equation B.6 will be reduced to

$$\epsilon_H = \phi_{npf}(E_n, L_{np}) n_H(E_n)\sigma_H. \tag{B.7}$$

The final results are plotted in Fig. B.8 that shows the neutron detection efficiency for the NE213 detector as a function of neutron energy for L_{np} corresponding to a neutron energy threshold of 5 MeV.

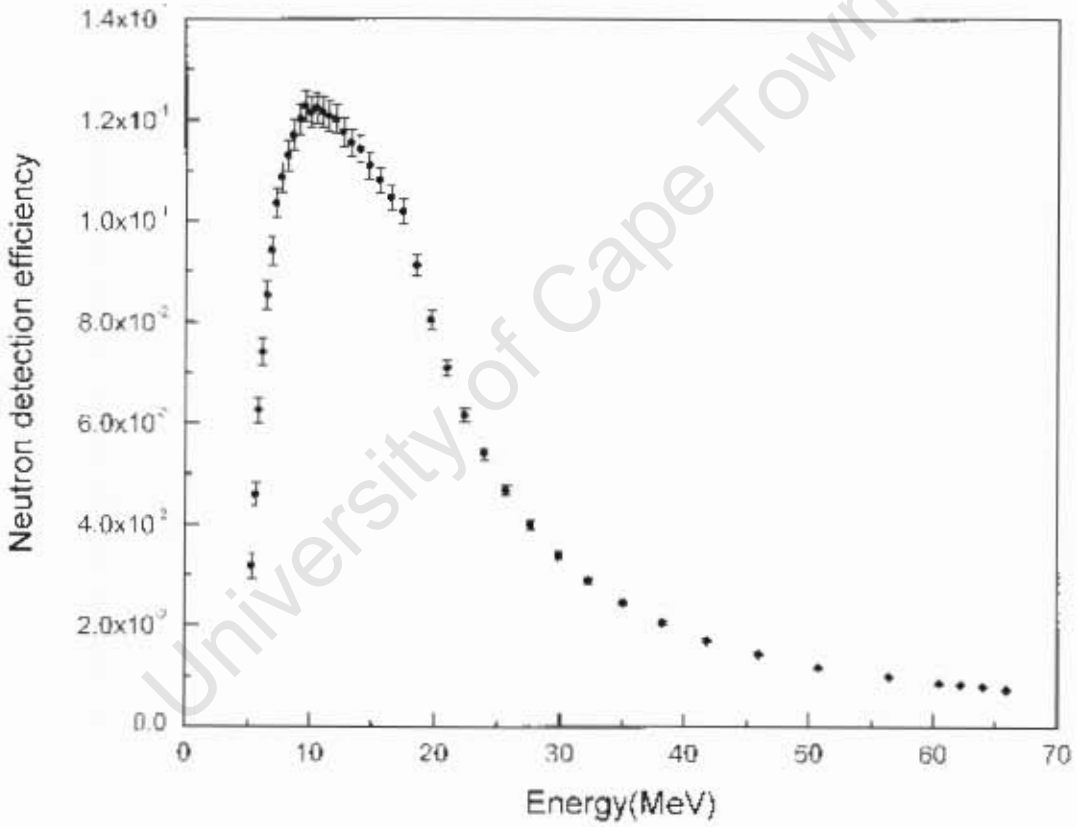

Figure B.8: Neutron detection efficiency for NE213 detector as a function of neutron energy for a detection neutron energy threshold 5 MeV [31].

Bibliography

[1] iThemba Laboratory for Accelerator Based Sciences. http://www.tlabs.ac.za.

[2] F. D. Brooks, A. Buffler, M. S. Allie, M. S. Herbert, M. R. Nchodu, D. T. L. Jones, F. D. Smit, R. Nolte, and V. Dangendorf. A compact High-energy Neutron Spectrometer. *Radiation Protection Dosimetry*, 126(1-5):218–222, 2007.

[3] R. Nolte, K. H. Mhlbradt, J.P. Meulders, G. Stephan, M. Haney, and E. Schmid. RBE of Quasi-monoenergetic 60 MeV Neutron Radiation for the Induction of Dicentric Chromosomes in Human Lymphocytes. *Radiation and environmental biophysics*, 44(3):201–209, 2005.

[4] J. M. Sisterson, F. D. Brooks, A. Buffler, M. S. Allie, D. T. L. Jones, and M. B. Chadwick. Cross-section Measurements for Neutron Induced Reactions in Copper at Neutron Energies of 70.7 and 110.8 MeV. *Nuclear Instruments and Methods in Physics Research*, 240(B):617–624, 2005.

[5] R. Nolte, M. S. Allie, P.J. Binns, F. D. Brooks, A. Buffler, V. Dangendorf, J.P Meulders, F. Roos, H. Schuhmacher, and B. Wiegel. High-energy neutron reference fields for the calibration of detectors used in neutron spectrometry. *Nuclear Instruments and Methods in Physics Research*, 476:369–373, 2002.

[6] R. Nolte, A. Buffler, and J.P. Slabbert. Relative Biological Efficiency of 192 MeV Neutron Radiation for the Induction of Chromosome Aberrations in Human Lymphocytes of the Peripheral Blood. *Proceedings of Science, International Workshop on Fast Neutron Detectors, University of Cape Town*, 2006.

[7] R. Nolte, V. Dangendorf, E.Schmid, J. P. Slabbert, G. Stephan, and F. D. Smit. RBE_M for the Induction of Dicentric Chromosomes in Human Lymphocytes by Quasi-monoenergetic 100 MeV and 200 MeV Neutron Radiation. *in Press*.

[8] A. Buffler, F.D. Brooks, M.S. Allie, P.J. Binns, V. Dangendorf, K.M. Langen, R. Nolte, and H. Schuhmacher. Measurement of neutron energy spectra from 15 to 150 MeV using stacked liquid scintillators. *Nuclear Instruments and Methods in Physics Research*, 476(1-2):181–185, 2002.

[9] N. Nakao, M. Nakao, H. Nakashima, S. Tanaka, Y. Sakamoto, Y. Nakane, and T. Nakamura. Measurements and Calculations of Neutron Energy Spectra Behind Polyethylene Shields Bombarded by 40- and 65-MeV Quasi-Monoenergetic Neutron Sources. *Nulear Science and Technology*, 34(4):348–359, 1997.

[10] iThemba LABS, J. L. Conradie, P. J. Celliers, P. A.Crafford, J. G. de Villiers, J. L. Delsink, H. du Plessis, Z. Kormany, R. E. Fenemore, D. T. Fourie, Y. E. Manjoo, T. N. Van der Walt, J. T. Van der Walt, G. S. Price, G. S. Price, J. F. Sharpey-Schafer, G. F. Steyn, and M. J. Van Niekerk. Cyclotrons at iThemba LABS. *iThemba LABS website: http:/www.tlabs.ac.za*.

[11] iThemba LABS, J. L. Conradie, P. J. Celliers, J. G. de Villiers, J. L. Delsink, H. du Plessis, J. H. du Toit, R. E. Fenemore, D. T. Fourie, I. H. Kohler, C. Lussi, P. T. Mansfield, H. Mostert, G. S. Muller, G. S. Price, P. F. Rohwer, M. Sakildien, R. W. Thomae, M. J. Van Niekerk, and P. A. Van Schalkwyk. Improvements of the iThemba LABS Cyclotron Facility. *Cyclotrons and their Applications, Eighteenth International Conference*, 2007.

[12] H. Schuhmacher, H. J. Brede, V. Dangendorf, M. Kuhfuss, J.P. Meulders, W. D. Newhauser, and R. Nolte. Quasi-monoenergetic neutron beams with energies from 25 to 70 MeV. *Nuclear Instruments and Methods in Physics Research*, 421(A):284–295, 1999.

[13] F. D. Brooks and H. Klein. Neutron spectrometry - historical review and present status. *Nuclear Instruments and Methods in Physics Research*, 476(A):1–11, 2002.

[14] R. Nolte, H. Schuhmacher, H. J. Brede, and U. J Schrewe. Measurement of High Energy Neutron Fluence with Scintillation Detector and Proton Recoil Telescope. *Radiation Protection Dosimetry*, 44:101–104, 1992.

[15] I. V. Ryzhov, G. A. Tutin, A. G. Mitryukhin, V. S. Oplavin, S. M. Soloviev, J. Blomgren, P. U. Renberg, J. P. Meulders, Y. E. Masri, T. Keutgen, R. Prieels, and R. Nolte. Measurements of neutron-induced fission cross-sections of ^{205}Tl, ^{204,206,207,208}Pb and ^{209}Bi with a multi-section Frisch-gridded ionization chamber. *Nuclear Instruments and Methods in Physics Research*, 562(A):439–448, 2006.

[16] Glenn F.Knoll. *Radiation Detection and Measurement*. John Wiley, Sons, 1979.

[17] H. Klein and S. Neumann. Neutron and photon spectrometry with liquid scintillation detectors in mixed fields. *Nuclear Instruments and methods in physics research*, A(476):132–142, 2002.

[18] J.M. Adams and G. White. A versatile Pulse Shapes Discriminator for Charge Particle Separation and its Application to Fast Neutron Time of Flight Spectroscopy. *Nuclear Instrument and Methods*, 156:459–476, 1978.

[19] F. D. Smit. The photodisintegration of the deuteron close to threshold. *University of Cape Town*, PhD thesis, 1986.

[20] F. D. Smit and F.D. Brooks. Angular Distribution of Neutrons from ^{2}H(γ, n)^{1}H at E_γ = 2.75 MeV. *Radiation Protection Dosimetry*, 465(A):429–444, 1987.

[21] N. Nakao, T. Kurosawa, T. Nakamura, and Y. Uwamino. Development of a quasi-monoenergetic neutron field and measurements of the response function of an organic liquid scintillator for the neutron energy range from 66 to 206 MeV. *Nuclear Instruments and Methods in Physics Research*, 476:176–180, 2002.

[22] N. Nakao, T. Kurosawa, T. Nakamura, and Y. Uwamino. Measurements of the response function of an organic liquid scintillator for the neutron energy range up to 135 MeV. *Nuclear Instrument and Methods in Physics Research*, 362:454–465, 1995.

[23] J. Thun, J. Blomgrena, K. Elmgren, J. Kallne, N. Olsson, J.F. Lecolley, F. Lefebvres, C. Varignon, F. Borne, X. Ledoux, Y. Patin, O. Jonsson, and P. U. Renberg. The response function of a liquid scintillator detector to 21-100 MeV neutrons. *Nuclear Instrument and Methods in Physics Research*, 478:559–576, 2002.

[24] S. Meigo. Measurements of the response function and the detection efficiency of an NE213 scintillator for neutrons between 20 and 65 MeV. *Nuclear Instruments and Methods in Physics Research*, 401:365–378, 1997.

[25] J.A. Lockwood, C. Chen, L.A. Friling, D. Swartz, R.N. St. Onge, A. Galonsky, and R.R. Doering. Response functions of organic scintillators to high energy neutrons. *Nuclear Instruments and Methods in Physics Research*, 138:353–362, 1976.

[26] K. Shin, Y. Ishii, Y. Uwamino, H. Sakai, and S. Numata. Measurements of NE213 response functions to neutrons of energies up to several tens of MeV. *Nuclear Instruments and Methods in Physics Research*, 308:609–615, 1991.

[27] N. Nakao, T. Kurosawa, T. Nakamura, and Y. Uwamino. Absolute measurements of the response function of an NE213 organic liquid scintillator for the neutron energy range up to 206 MeV. *Nuclear Instruments and Methods in Physics Research*, 463(A):275–287, 2001.

[28] Kenneth S. Krane. *Introductory Nuclear Physics*. John Wiley, Sons, 1987.

[29] E. Segre P. Morrison, B. T. Feld. *Experimental Nuclear Physics*, volume 2. John Wiley, Sons, 1953.

[30] M. Sasaki, N. Nakao, T. Nakamura, T. Shibata, and A. Fukumura. Measurements of the response functions of an NE213 organic liquid scintillator to neutrons up to 800 MeV . *Nuclear Instruments and Methods in Physics Research*, 480(A):440–447, 2002.

[31] M. Herbert. Determination of Neutron Energy Spectra Inside a Water Phantom Irradiated by Neutrons of Energy up to 64 MeV. *University of Cape Town*, PhD thesis, 2009.

[32] S. Meigo, H. Takada, and S. Chiba et al. Measurements of neutron spectra produced from a thick lead target bombarded with 0.5 and 1.5 GeV. *Nuclear Instruments and methods in physics research*, A(431):521–530, 1999.

[33] A. V. Alevra. Neutron Spectrometry. *Radio-protection*, 34(4):305–333, 1999.

[34] Database Version of August 10 2009 International Atomic Energy Agency, Nuclear Data Services. *Evaluated Nuclear Data File (ENDF)*. http://www-nds.iaea.org.

[35] F.D. Brooks, M.S. Allie, A. Buffler, V. Dangendorf, M. S. Herbert, S. A. Makupula, R. Nolte, and F. D. Smit. Measurement of neutron fluence spectra up to 150 MeV using a stacked scintillator neutron spectrometer. *Radiation Protection Dosimetry*, 110:151–155, 2004.

[36] M. Matzke. Propagation of Uncertainties in Unfolding Procedures. *Nuclear Instruments and Methods in Physics Research*, 476:230–241, 2002.

[37] J.F. Briesmeister, editor. *MCNP A general Monte Carlo N-Particle transport code, version 4c, LA-13709M.* Los Alamos National Laboratory, USA, 2000.

[38] Webots. Mcnp - a general monte carlo n-particle transport code. `http://mcnp-green.lanl.gov/index.html`.

[39] B. Pelowitz, editor. *MCNPX User's Manual, Version 2.5.0.* Los Alamos National Laboratory, LA-CP-05-0369, 2005.

[40] S. Agostinelli et al. Geant4 - A Simulation Toolkit. *Nuclear Instruments and methods*, A(506):250–303, 2003.

[41] Geometry and Tracking Code (GEANT4). Official website. `http://geant4.cern.ch`.

[42] A. Fasso, A. Ferrari, J. Ranft, and P. R. Sala. *FLUKA Code.* 2006.

[43] FLUKA Developer Group. http://www.fluka.org. The use of FLUKA.

[44] M. B. Emmet. The Morse Monte Carlo Radiation Transport System. *Oak Ridge National Laboratory, ORNL*, 1974.

[45] A. Ferrari and P. Sala. The Physics of High Energy Reactions. *Workshop on Nuclear Reaction Data and Nuclear Reactors, International Center for Theoretical PhysicsTrieste, Italy*, (Proceeding in press), 1996. Obtained on March 2009 from: `http://www.fluka.org`.

[46] A. Ferrari and P. Sala. A New Model for Hadronic Interactions at Intermediate Energies for the FLUKA Code. *Official FLUKA site: publication data base*, 2006.

[47] J. Ranft. FLUKA: Performance and Applications in the Intermediate Energy Range. *Physical Review D*, 51(1), 1994.

[48] E. Gadioli, F. Cerutti, F. Ballarini, and G. Battistoni et al. The FLUKA code: An Overview. *Journal of Physics: Conference Series*, pages 151–160, 2006.

[49] A. Fasso, S. Roesler, V. Andersen, F. Ballarini, and G. Battistoni et al. The FLUKA code: Present Application and Future Developments. *Computing in High energy and Nuclear Physics*, 2003.

[50] F. Ballarini, G. Battistoni, and F. Cerutti et al. Nuclear Models in FLUKA: Present capabilities, open problems and future improvements. *International Conference on Nuclear Data for Science and Technology (ND2004) - Santa Fe, NM*, 2004.

[51] G. Collazuol, A. Ferrari, A. Guglielmi, and P. Sala. Hadronic models and experimental data for the neutrino beam production. *Nuclear Instruments and methods in physics research*, A(449):609–623, 2000.

[52] F. Ballarini, G. Battistoni, M. Brugger, and et al. The Physics of the FLUKA Code: Recent Developments. *Advances in Space Research*, 40:1339–1349, 2007.

[53] A. Fasso, A. Ferrari, J. Ranft, and P. Sala. New developments in FLUKA modelling of hadronic and EM interactions. *Official FLUKA site: publication data base.*, page 32, 1997.

[54] A.Fasso, A. Ferrari, and P. Sala. Electron-Photon Transport in FLUKA: status. *Proc. of Advanced Monte-Carlo for Radiation Physics, Particle Transport Simulation and Applications*, pages 159–164, 2000.

[55] A. Fasso, P.R. Sala, F. Ballarini, and Battistoni G. The Physics Models of FLUKA: Status and Recent Developments. *Computing in High Energy and Nuclear Physics (CHEP03)*, 2003.

[56] B. Pastircak. FLUKA MONTE CARLO Simulation Code Used for Radiation Studies in ALICE Experiment. *Physics of Particle and Nuclei Letter*, 5(3):301–304, 2008.

[57] A. Ferrari, P. Sala, R.Guaraldi, and F. Padoani. An improved multiple scattering model for charged particle transport. *Nuclear Instruments and Methods in Physics Research*, 71(B):412–426, 1992.

[58] M. S. Herbert, F.D. Brooks, M.S. Allie, A. Buffler, M. R. Nchodu, S. A. Makupula, D. T. L. Jones, and K. M. Langen. Determination of Neutron Energy Spectra Inside A water Phantom Irradiated by 64 MeV Neutrons. *Radiation Protection Dosimetry*, 126(1-4):346–349, 2007.

[59] P. Jipsen and J. Maritz. Program ELOSS 2.0, based on data from H. H. Andersen and J. F. Ziegler in the stopping and Range of Ions in Matter. *Pergamon Press, New York*, 3, 4 and 5, 1977.

[60] A. Buffler. The Response of Organic Scintillators to Neutrons of Energy 14-63 MeV. *University of Cape Town*, M.Sc thesis, 1990.

[61] P. F. Rose. ENDF/B-VI Summary Documentation, Report BNLNCS - 17541. *Brookhaven National Laboratory*, 1991.

[62] International Organization for Standardization, Guide to the Expression of Uncertainty in Measurement. *Geneva, Switzerland*, 1995.

[63] N. Barry and E. Kuyatt. Guidelines for Evaluating and Expressing the Uncertainty of NIST Measurement Results, NIST Technical Note 1297. *National Institute of Standards and Technology*, 1994.

[64] L. Blumberg and S. Schlesinger. Kinematics of the relativistic two body problem. *Report LAMS-1718-C3, Los Alamos National Laboratory*, 1955.

[65] Nicholas Tsoulfanidis. *Measurement and Detection of Radiation.* Washington, DC,Taylor and Francis, 1995.

[66] M. Reginatto, P. Goldhagena, and S. Neumann. Spectrum unfolding, sensitivity analysis and propagation of uncertainties with the maximum entropy deconvolution code MAXED. *Nuclear Instruments and Methods in Physics Research*, 476(A):242–246, 2002.

[67] M. Reginatto and P. Goldhagen. MAXED, A COMPUTER CODE FOR MAXIMUM ENTROPY DECONVOLUTION OF MULTISPHERE NEUTRON SPECTROMETER DATA. *Health Physics*, 77(5):579–583, 1999.

[68] S. Makupula. Measurement of Spectral Neutron Fluence from 5-200 MeV by Means of Liquid Scintillators. *University of Cape Town*, M.Sc thesis, 2003.